RSC Advances

PAPER

View Article Online
View Journal | View Issue

Cite this: *RSC Adv.*, 2026, **16**, 18591

Synergistic effects of Fe species distribution and acid site balance in Fe/zeolite catalysts for 5-HMF production from glucose

Tatchapol Nanmong,[a] Waranya Obrom,[a] Worapol Yingyuen,[a] Tanawat Jaroenchur,[a] Phatteenan Thamthong,[a] Jatuporn Wittayakun,[b] Sanchai Prayoonpokarach,[b] Pimrapus Tawachkultanadilok,[c] Yingyot Poo-arporn,[c] Suttipong Wannapaiboon,[c] Narong Chanlek,[c] Bunyarat Rungtaweevoranit,[d] Siriporn Kosawatthanakun,[d] Pongtanawat Khemthong,[d] Jean-Paul Desaulniers[e] and Sirinuch Loiha *[a]

The selective conversion of glucose to 5-hydroxymethylfurfural (5-HMF) remains a key challenge in biomass valorization due to the complex interplay between Brønsted and Lewis acid sites. In this work, iron-supported HMOR and HZSM-5 zeolites were synthesized and systematically investigated to elucidate the roles of acid site nature, strength, and iron speciation in glucose conversion. Comprehensive characterization using XANES, UV-vis DRS, XPS, NH_3-TPD, and pyridine-IR revealed that Fe incorporation generates bifunctional catalysts containing Fe-based Lewis acid sites (Fe_2O_3 and Fe_3O_4) together with Brønsted acid sites derived from framework Si–OH–Al, surface Fe–OH, and extra-framework Al–OH species. Py-IR analysis showed that Fe/HMOR exhibits a higher Brønsted/Lewis (B/L) acid ratio than Fe/HZSM-5 due to the formation of oligomeric and hydrated Fe species. Catalytic evaluation in a biphasic n-butanol/water system demonstrated that moderate acidity and an optimized B/L ratio are critical for enhancing 5-HMF selectivity while suppressing levulinic acid formation. The highest 5-HMF yield (~44–45%) was achieved with 6Fe/HMOR at 190 °C, which correlated strongly with a high fraction of Fe_3O_4 species. These findings provide mechanistic insight into acid site synergy and offer design principles for improved glucose to 5-HMF catalysts.

Received 16th January 2026
Accepted 16th March 2026

DOI: 10.1039/d6ra00413j

rsc.li/rsc-advances

1 Introduction

As demand for fine chemicals continues to rise, the production of energy and petroleum-based products has increased accordingly, raising concerns about the depletion of fossil fuels and environmental pollution. In response, biomass has gained attention as a renewable and sustainable alternative for producing value-added chemicals, reflecting a broader societal shift toward environmental responsibility and economic sustainability. Recent studies indicate that while 5-hydroxymethylfurfural (5-HMF) can be efficiently produced from fructose, its high cost limits commercial viability. Glucose, being more abundant and cost-effective, is derived from lignocellulosic biomass.[1–3] The conversion of glucose to 5-HMF involves isomerization to fructose, typically using Lewis acids, followed by Brønsted acid-catalyzed dehydration. However, side reactions can produce unwanted byproducts, such as levulinic acid and formic acid.[4] To improve catalytic efficiency, both homogeneous and heterogeneous catalysts have been studied. While homogeneous acids, such as HCl, can be effective, they face challenges in separation and high energy consumption.[5] Heterogeneous catalysts, excellent acids such as metal oxides and zeolites, are preferred due to their selectivity and ease of recovery.[6] Recent studies have shown that sulfonic acid ($-SO_3H$) functionalized solid acids as the heterogeneous catalysts, such as carbon-based materials, mesoporous silicas, and hybrid composites, exhibit remarkable catalytic performance for the dehydration of glucose and fructose to 5-HMF, achieving yields as high as 98% under optimized conditions.[7–9] These catalysts combine high Brønsted acidity, tunable pore architectures, and excellent thermal stability, while solvent effects and acid-site accessibility are crucial for improving selectivity and suppressing humin formation. Furthermore, the immobilization of $-SO_3H$ groups or sulfonated ionic liquids on ordered mesoporous supports such as SBA-16 has been demonstrated to

[a]*Center of Excellence for Innovation in Chemistry, Department of Chemistry, Faculty of Science, Khon Kaen University, Khon Kaen, Thailand. E-mail: Sirilo@kku.ac.th*
[b]*School of Chemistry, Institute of Science, Suranaree University of Technology, Nakhon Ratchasima, Thailand*
[c]*Synchrotron Light Research Institute (public organization), Nakhon Ratchasima, Thailand*
[d]*NanoCatalysis and Molecular Simulation Research Group, National Nanotechnology Center (NANOTEC), National Science and Technology Development Agency (NSTDA), Pathumthani, Thailand*
[e]*Faculty of Science, Ontario Tech University, 2000 Simcoe Street North, Oshawa, Ontario L1G 0C5, Canada*

enhance both catalytic efficiency and recyclability, offering a promising route toward sustainable 5-HMF production.[9]

Porous materials, especially microporous and mesoporous structures, enhance sugar conversion by improving mass transfer in fructose dehydration.[10] Zeolites possess a well-defined crystalline structure with a porous architecture, allowing for controlled modification of Brønsted acidity through the framework composition and Lewis acidity *via* specific iron speciation; however, research in this area is sparse and warrants investigation.[10,11] The acid sites present in these zeolites play a crucial role: Lewis acid sites facilitate the conversion of glucose to fructose, while Brønsted acid sites catalyze the subsequent dehydration process to produce 5-HMF. Thus, both Lewis and Brønsted acid sites are essential for efficient conversion of glucose.[12–14] Additionally, incorporating metals such as Sn, Cr, Al, and Fe into zeolite frameworks can enhance acidity, thereby aiding both isomerization and dehydration.[15–17] The incorporation of iron into zeolite frameworks results in the formation of distinct iron oxide structures, which significantly impact glucose conversion efficiency and 5-HMF selectivity. At low Fe loadings (1–3 wt%), iron is predominantly found as isolated Fe^{3+} species in extra-framework positions, exhibiting firm Lewis acidity that is vital for the isomerization of glucose to fructose.[18,19] A recent review on acid–base bifunctional catalysts for 5-HMF production highlights the importance of synergistic active sites and rational design in achieving up to 93% glucose to 5-HMF yields. It emphasizes balancing hydrolysis, isomerization, and dehydration to enhance catalytic efficiency. These insights inform the design of our iron-supported zeolite catalysts, where the interaction between Fe species and zeolitic acid sites may enhance 5-HMF production while ensuring structural stability.[20]

However, as Fe loading increases beyond 5 wt%, the emergence of α-Fe_2O_3 (hematite) clusters becomes more prevalent, especially in large-pore zeolites such as HY and β-zeolite. These clusters exhibit weak Lewis acidity and tend to catalyze glucose degradation to levulinic acid rather than promoting the productive formation of 5-HMF.[19] In contrast, the presence of Fe_3O_4 (magnetite) species, characterized by mixed Fe^{2+}/Fe^{3+} oxidation states, shows superior activity in glucose isomerization due to enhanced Lewis acid sites that promote the activation of C–O bonds.[21] The topology of the zeolite framework plays a crucial role in determining the speciation of iron. HMOR and HZSM-5 were chosen as zeolite supports due to their different frameworks and pore architectures, which allow for an evaluation of how these structures affect iron species distribution and acid site balance. HMOR has one-dimensional 12-membered-ring channels and large pores, promoting the aggregation and hydration of metal species. In contrast, HZSM-5 features a three-dimensional system of 10-membered rings that restricts metal mobility and stabilizes isolated oxide species. For instance, the medium-pore structure of HZSM-5 constrains the growth of Fe_2O_3 clusters, leading to better dispersion of active Fe^{3+} species. Meanwhile, the one-dimensional, large pores of HMOR may facilitate Fe clustering while also providing excellent accessibility for glucose.[17,21]

Biphasic solvent systems have been studied to enhance process efficiency and stability, thereby allowing better control of reaction conditions and improving product yield. The exploration of organic solvents could also expand the range of substrates and optimize production.[22,23] In these systems, an immiscible organic solvent facilitates phase separation, enabling the generation of 5-HMF *via* dehydration reactions of glucose in the aqueous phase. Organic solvents like tetrahydrofuran (THF),[24] ethyl acetate,[25] dimethyl sulfoxide (DMSO),[26] and butyl alcohol (BuOH)[27] effectively extract 5-HMF from the aqueous phase and reduce its degradation. THF-based systems, although achieving respectable yields (42–65%), are plagued by volatility (b.p. 66 °C), resulting in solvent loss, safety concerns due to peroxide formation, and difficulties in maintaining stable biphasic conditions over extended reaction periods.[17,28,29] DMSO/water systems exhibit excellent 5-HMF extraction efficiency (80–90%) due to the high polarity of DMSO and the capacity to solvate glucose; however, the high boiling point (189 °C) necessitates energy-intensive separation processes. Additionally, the viscosity of DMSO contributes to mass-transfer limitations that reduce overall reaction rates.[18,28] Acetone-based biphasic systems suffer from poor phase-separation stability and have limited 5-HMF extraction capacity (50–60%), while ethyl acetate systems experience catalyst deactivation due to ester hydrolysis under acidic reaction conditions.[30] The salting-out effect, typically achieved with NaCl or KCl, enhances 5-HMF partitioning into organic phases by decreasing its aqueous solubility, yet optimizing salt concentration remains a challenge across various solvent systems.[31,32] The proposed *n*-BuOH/aq. NaCl biphasic system addresses these limitations by providing optimal polarity (μ = 1.63 D) for effective 5-HMF extraction while maintaining a clear phase.

Supported metal catalysts (Fe/HZSM-5 and Fe/HMOR) were synthesized by impregnating Fe^{3+} onto HZSM-5 and HMOR zeolites. Rice husk served as the biomass feedstock for preparing the zeolites, which were synthesized using hydrothermal methods. Before using the catalysts for glucose conversion to 5-HMF, we characterized their physicochemical properties. The catalytic conversion of glucose was monitored by high-performance liquid chromatography (HPLC), and the yield and product distribution of 5-HMF were analyzed in relation to catalyst properties and the iron species formed on the different zeolite types.

2 Experiments

2.1 Materials

Rice husk was collected from agricultural waste (local supplier, Thailand) and used as the silica source. Sodium hydroxide (NaOH, ≥98%, Merck), sodium aluminate ($NaAlO_2$, technical grade, Sigma-Aldrich), tetrapropylammonium bromide (TPABr, ≥98%, Sigma-Aldrich), ammonium nitrate (NH_4NO_3, ≥99%, Merck), tetrahydrofuran (THF, ≥99.5%, HPLC grade, Sigma-Aldrich), iron(III) nitrate hexahydrate ($Fe(NO_3)_3 \cdot 6H_2O$, ≥98%, Sigma-Aldrich), D-glucose (≥99%, Sigma-Aldrich), sodium chloride (NaCl, ≥99%, Merck), *n*-butanol (*n*-BuOH, ≥99%, Merck), hydrochloric acid (HCl, 37%, ACS reagent, Sigma-

Aldrich), and sulfuric acid (H_2SO_4, 95–98%, ACS reagent, Merck) were used as received without further purification.

2.2 Silica extraction from rice husk

Rice husk was thoroughly washed and dried with distilled water, then dried at 80 °C overnight. A total of 100 g of the dried rice husk was refluxed with 3 M HCl in a round-bottom flask using a microwave-assisted method at 600 W for 2 h. After refluxing, the rice husk was washed with distilled water until the pH reached neutrality, then dried overnight at 80 °C. Finally, the rice husk was calcined at 450 °C to extract silica.

2.3 Synthesis of NaZSM-5 zeolite

NaZSM-5 was synthesized using a hydrothermal method. The process began by dissolving 8.64 g of silica in a NaOH solution prepared by mixing 10.34 g of NaOH with 60 mL of deionized (DI) water. This was followed by the sequential addition of 0.81 g of $NaAlO_2$ in 50 mL of DI water and 5.9 g of TPABr in 23.5 mL of DI water, which served as the structure-directing agent. The pH of the mixture was adjusted to 9–11 using 2 M H_2SO_4. The resulting gel was hydrothermally treated at 170 °C for 72 h in a Teflon-lined autoclave. Afterward, it was washed to a neutral pH, dried, and calcined at 550 °C for 5 h, yielding NaZSM-5 as a fine, white powder.

2.4 Synthesis of NaMOR zeolite

NaMOR zeolite was synthesized by first dissolving 18.00 g of silica in a NaOH solution comprising 7.96 g NaOH in 80 mL of DI water. This was followed by the addition of 2.46 g of $NaAlO_2$, dissolved in diluted H_2SO_4, and 12.17 mL of THF. The pH of the mixture was adjusted to 9–11 using 2 M NaOH. The resultant gel was hydrothermally treated at 180 °C for 72 h in a Teflon-lined autoclave. Afterward, it was washed to achieve a neutral pH, dried, and calcined at 550 °C for 5 h to yield NaMOR as a fine white powder.

2.5 HZSM-5 and HMOR preparation

The sodium forms of the zeolites (NaZSM-5 and NaMOR) were transformed into their protonic counterparts (HZSM-5 and HMOR) through ion exchange with ammonium ions. This was achieved by refluxing 1 g of the corresponding sodium zeolite in 30 mL of 1.25 M NH_4NO_3 solution at 70 °C for 6 h. The process involved centrifugal washing at 3500 rpm for 3 min, followed by drying and calcination to form proton-form zeolites.

2.6 Preparation of iron-supported catalysts

The section on iron-supported catalysts has been developed to address both 2% and 6% iron-loading preparations. For the 2% preparation, 0.17 g of $Fe(NO_3)_3 \cdot 6H_2O$ was dissolved in 4 mL of deionized water until a clear solution was obtained. Similarly, for the 6% preparation, 0.52 g of $Fe(NO_3)_3 \cdot 6H_2O$ was used. This iron solution was then gradually added to 2 g of the previously synthesized HZSM-5 and HMOR support. The mixture was dried on a hot plate at 80 °C for 24 h. The dried samples were finely milled using a mortar and subsequently calcined in a muffle furnace at 450 °C for 4 h to yield the 2Fe/HZSM-5, 6Fe/HZSM-5, 2Fe/HMOR, and 6Fe/HMOR catalysts.

2.7 Catalytic conversion of glucose to 5-HMF

Catalytic activity was assessed by measuring glucose conversion through the following procedure: 0.2 g of glucose, 0.2 g of catalyst, and 5 g of NaCl were mixed in a biphasic solvent system comprising 25 mL of DI water and 25 mL of n-butanol. This mixture was stirred vigorously until a clear solution was achieved. The reaction mixture was transferred to an autoclave and heated to varying temperatures for 4 h. After the reaction, the product solution was filtered through filter paper to separate the reaction products from the catalyst for further analysis. The resulting filtrate, containing the reaction products, was subsequently passed through a 0.22 μm microfilter to separate the organic solvent and aqueous phases.

The elemental composition of the products and the glucose conversion were determined *via* HPLC (GPC, Agilent Technologies) with a refractive index (RI) detector and a Hiplex-H column. The column temperature was maintained at 50 °C, and a flow rate of 0.550 mL min^{-1} was used with an aqueous sulfuric acid solution as the mobile phase. The conversion of glucose, product yield, and selectivity were analyzed and calculated using the following eqn (1)–(3), respectively.

$$\%\ \text{Glucose conversion} = \frac{\text{Moles of initial glucose} - \text{Moles of remaing glucose}}{\text{Moles of initial glucose}} \times 100\% \quad (1)$$

$$\%\ \text{5-HMF yield} = \frac{\text{Moles of obtained 5-HMF}}{\text{Moles of initial glucose}} \times 100\% \quad (2)$$

$$\%\ \text{LA yield} = \frac{\text{Moles of obtained LA}}{\text{Moles of initial glucose}} \times 100\% \quad (3)$$

2.8 Characterization

The crystalline structures of the synthesized materials were confirmed using a PANalytical EMPYREAN Powder X-ray Diffractometer (XRD). Structural confirmations of the materials were determined by using the Fourier-Transform Infrared Spectrometer (FT-IR), Bruker in the TENSOR27 model. Diffuse reflectance UV-visible (DR UV-vis) spectra were obtained in the range of 200–800 nm using a Shimadzu UV-VIS-NIR3101PC scanning spectrophotometer. 0.2 g of the sample was loaded into a holder covered with a quartz cell, and $BaSO_4$ was used as the reference material. Temperature-Programmed Desorption (TPD) was performed under pure NH_3 at an adsorption pressure of 100 mbar. TPD was performed in a vacuum system. Moreover, 50 mg of the pure sample was heated at a ramp rate of 5 °C min^{-1}. The produced gas was analyzed using mass spectrometry (MS; Pfeiffer Vacuum QMA 200 with a tungsten filament and a SEM detector). The oxidation state and speciation of the iron species were determined by X-ray absorption spectroscopy (XAS) and provided at BL1.1W, Synchrotron Light

Research Institute (SLRI) in the intermediate photon energy range of 7.0–8.0 keV for Fe K-edge, respectively. The chemical states of Fe, O, Si, and Al were analyzed using X-ray photoelectron spectroscopy ((XPS), PHI5000 VersaProbe II, ULVAC-PHI, Japan) at BL 5.3, the SUT-NANOTEC-SLRI Joint Research Facility, Synchrotron Light Research Institute (SLRI), Thailand. The composition and thermal stability of the catalysts were determined using TGA on a thermal analyzer (Netzsch-Gerätebau GmbH-STA 409 PC Luxx Simultaneous). Small samples (30 mg) were heated from RT to 700 °C at 10 °C min^{-1} in air and nitrogen. *In situ* diffuse reflectance infrared Fourier transform spectroscopy (DRIFTS) of adsorbed pyridine was collected in the range of 4000–400 cm^{-1} using a Nicolet FTIR spectrometer (64 scans, 4 cm^{-1} resolution). Samples were activated at 400 °C under vacuum (10^{-3} Torr) for 2 h, cooled to 50 °C, and a background spectrum was recorded. Pyridine was adsorbed at 50 °C until saturation, then the sample was evacuated to remove excess pyridine. Desorption was performed under vacuum at 100–250 °C, with spectra recorded at each temperature after 10 min holding. Pyridine adsorption spectra were obtained by subtracting the background spectrum.

3 Results and discussion

3.1 Catalyst structures

3.1.1 X-ray diffraction (XRD). The XRD patterns of the Fe-modified zeolite catalysts are presented in Fig. 1. The diffractograms of HMOR (Fig. 1a) exhibit characteristic peaks at $2\theta = 6.5°$, 9.8°, 19.6°, 22.3°, 25.6°, and 27.7°, confirming the typical MOR structure with orthorhombic symmetry.[33] In contrast, the HZSM-5 samples (Fig. 1b) display characteristic peaks at $2\theta = 7.9°$, 8.8°, 23.1°, 23.9°, and 24.4°, associated with the MFI topology.[34] After iron modification, the primary peaks of the zeolite were maintained, indicating that the zeolite structures remained intact. Nonetheless, the intensities of these peaks changed subtly, particularly for the 6% Fe-loaded samples, suggesting a potential interaction between the iron species and the zeolite framework. Notably, the 2% Fe-loaded catalysts exhibited fewer distinct diffraction peaks associated with crystalline iron oxide phases (such as α-Fe_2O_3 at $2\theta = 33.2°$, 35.6°, and 54.1°), which is attributed to the well-dispersed iron species as small clusters or isolated ions.[35] Conversely, the 6Fe/HZSM-5 sample exhibited faint reflections indicative of Fe_2O_3,

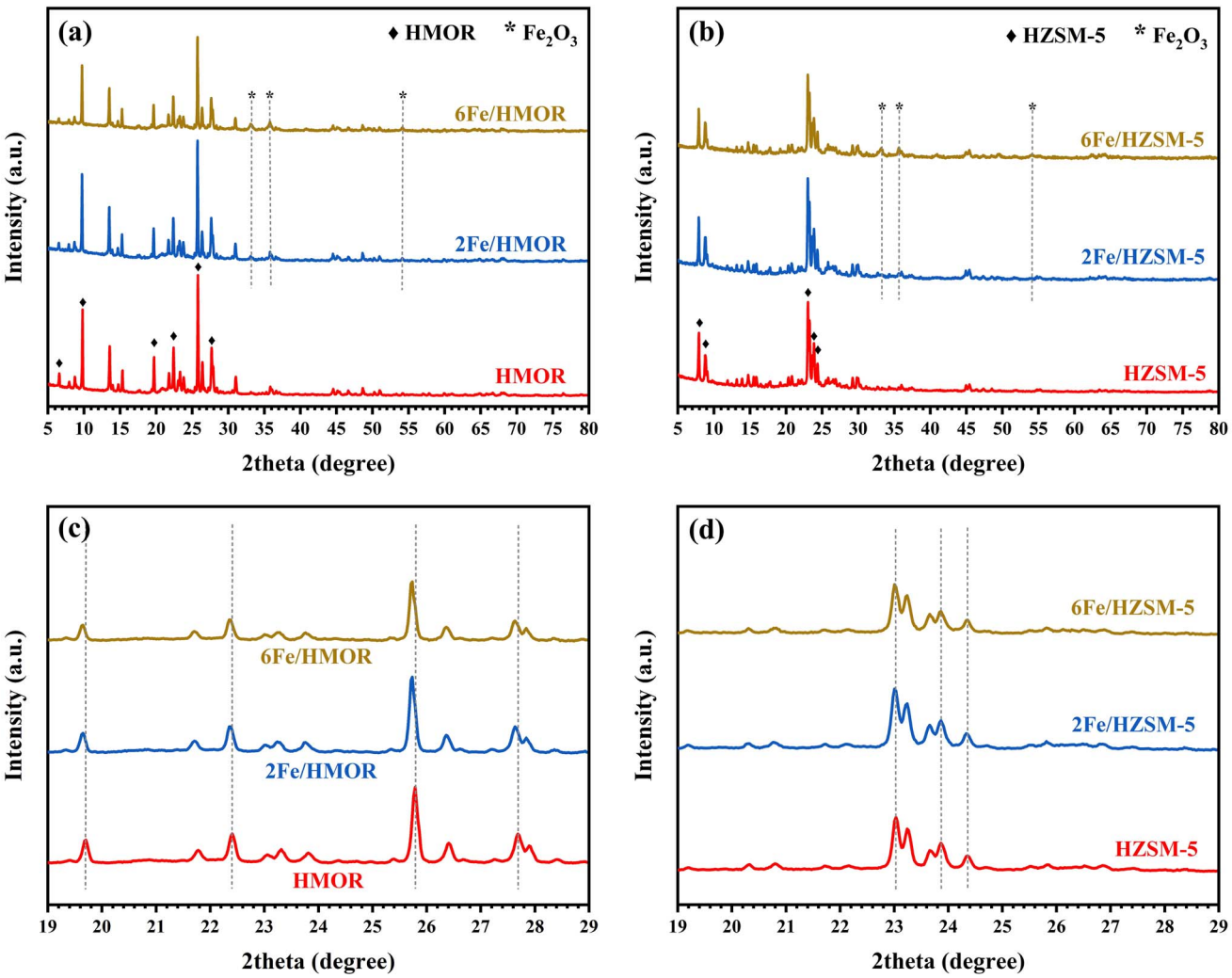

Fig. 1 The XRD patterns of Fe/HMOR (a), Fe/HZSM-5 (b) compared with the bare zeolites and their extended plot in the range of 19–29° (c and d).

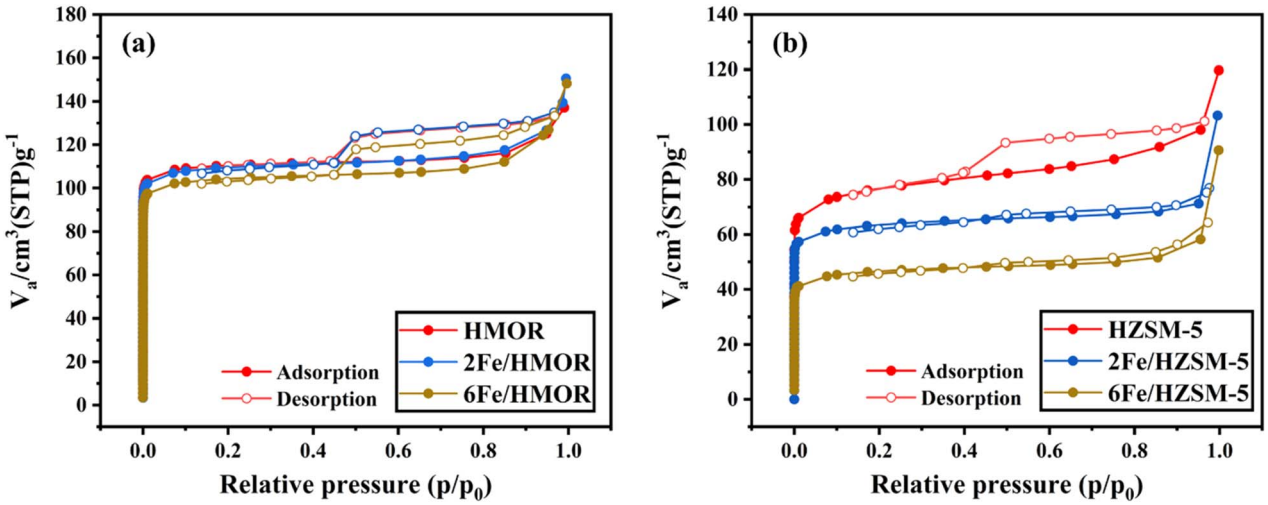

Fig. 2 N_2 adsorption–desorption isotherms of the Fe/HMOR (a) and Fe/HZSM-5 (b) catalysts compared with the bare zeolites.

implying the formation of larger iron oxide crystallites at increased Fe loadings.[36–38]

3.1.2 N_2-adsorption desorption. The N_2 adsorption–desorption isotherms of the catalysts are depicted in Fig. 2. Both the HMOR and HZSM-5 parent zeolites exhibited Type I isotherms with H4-type hysteresis loops, which are characteristic of microporous materials that also possess some mesoporosity.[39] A summary of the textural characteristics obtained from these isotherms is provided in Table 2. The BET surface area (SA) of HMOR was measured at 334 $m^2\ g^{-1}$, exceeding that of HZSM-5 (239 $m^2\ g^{-1}$), highlighting differences in their framework structures. However, the addition of Fe^{3+} supported on both zeolites resulted in a reduction in surface area, indicating partial pore blockage by iron species at higher loadings.[40] The average pore volume of the iron-modified catalysts decreased as the iron loading increased. Notably, the decrease in SA for Fe/HZSM-5 was more pronounced than that for Fe/HMOR, suggesting a higher degree of surface blocking by larger iron particles on HZSM-5. This observation correlates with the increase in iron oxide particles on Fe/HZSM-5, as confirmed by the UV-vis DRS analysis presented in Table 1. In contrast, the mesopore volume increased slightly with increasing iron loading. This observed increase in mesopore volume in the iron-modified HMOR and HZSM-5 samples can be attributed to some restructuring of the framework that occurs during the impregnation and calcination processes.[41]

3.1.3 Scanning electron microscopy-energy dispersive X-ray spectroscopy (SEM-EDS). The SEM micrographs and corresponding EDS analyses of the parent zeolites (HMOR and HZSM-5) and their iron-modified counterparts with varying iron loadings are shown in Fig. 3. The HMOR zeolite displays characteristic prismatic crystallites with a relatively uniform size distribution (Fig. 3a). In contrast, HZSM-5 consists of smaller, more cubic aggregated particles, which aligns with findings in the existing literature.[42,43] Significant morphological changes were observed after incorporating iron, resulting in a plate-like structure for Fe/HMOR. However, the aggregated cubic shape of Fe/HZSM-5 remained essentially unchanged compared to the pristine HZSM-5. The elemental distribution, analyzed through SEM-EDS (Fig. 3b), indicated a uniform distribution of iron across the zeolite supports. The surface iron content in Table 2 closely matched the calculated iron loading amount (2 wt% and 6wt% Fe). Interestingly, the Si/Al ratios for Fe/HMOR and Fe/ZSM-5 slightly increased with the addition of iron, suggesting partial dealumination of the zeolite structures. These results corresponded well with a decrease in peak intensity observed in the XRD analysis. Notably, the most significant increase in the Si/Al ratio was seen in the 2Fe/HZSM-5 sample, indicating the highest level of iron incorporation into the zeolite structure.

3.1.4 Fourier transform infrared spectroscopy (FTIR). The FTIR analysis of both the bare and Fe/zeolite catalysts is shown in Fig. 4, which highlights the characteristic framework vibrations corresponding to the internal asymmetric stretching of Si–

Table 1 The percent distribution of iron species on the catalysts provided by the decomposition of the UV-vis DRS spectra

Modified zeolites	I_1[a] [%] (λ < 300 nm)	I_2[b] [%] (λ = 300–450 nm)	I_3[c] [%] (λ = 450–600 nm)	I_4[d] [%] (λ > 600 nm)
2Fe/HMOR	57	29	14	0
6Fe/HMOR	35	59	4	2
2Fe/HZSM-5	53	27	20	0
6Fe/HZSM-5	58	13	28	1

[a] I_1 at λ < 300 nm → isolated Fe^{3+} in tetrahedral and octahedral coordination. [b] I_2 at λ = 300–450 nm → oligomeric Fe_xO_y and clusters. [c] I_3 at λ = 450–600 nm → small particles. [d] I_4 at λ > 600 nm → large particles.

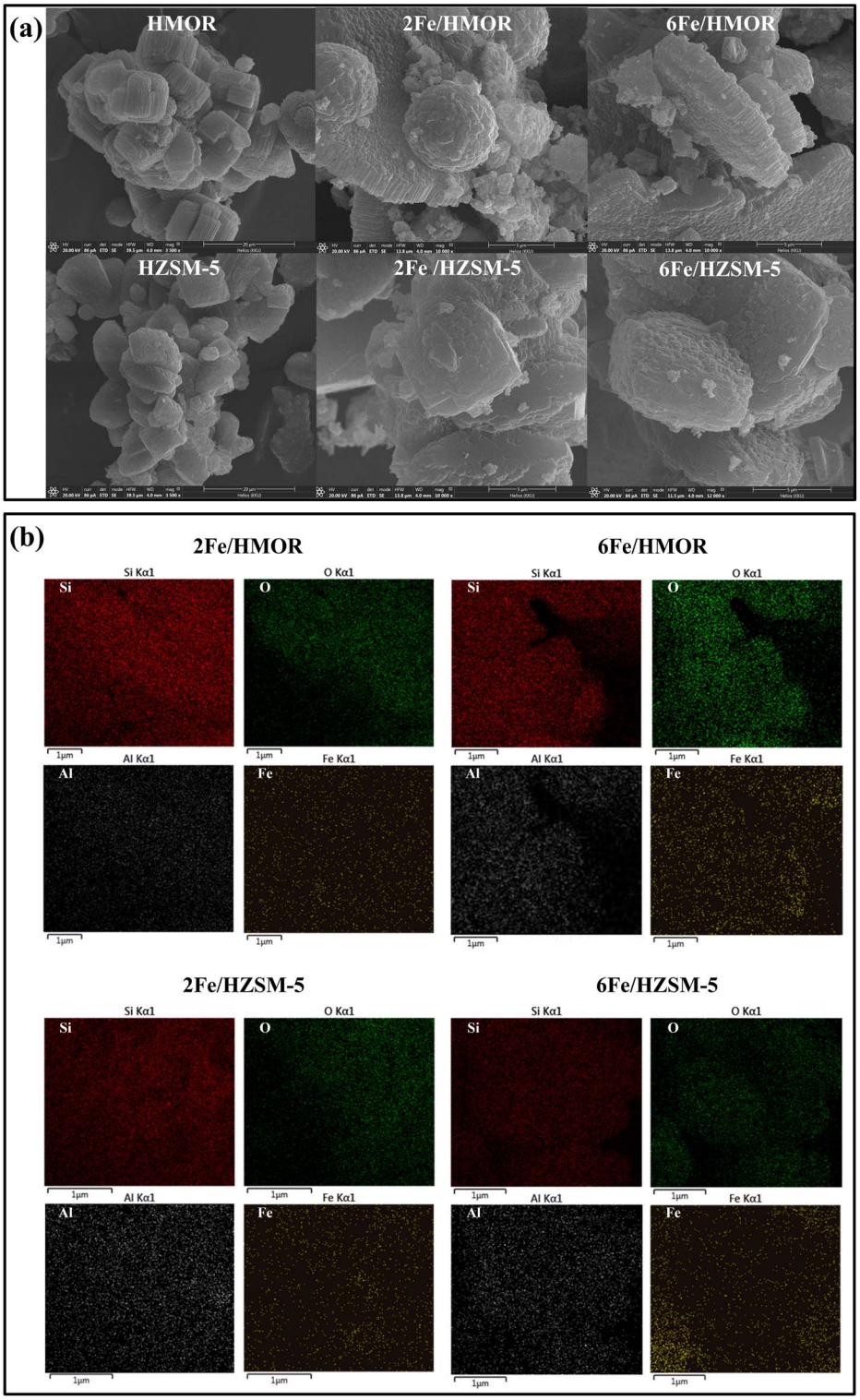

Fig. 3 SEM of HMOR, 2Fe/HMOR, 6Fe/HMOR, HZSM-5, 2Fe/HZSM-5, and 6Fe/HZSM-5 (a) elemental analysis by SEM-EDS of the catalysts (b).

O–T linkages, occurring in the range of approximately 1064–1100 cm^{-1}. This is specifically related to the TO_4 (where T can be Si or Al) units in the zeolite structures. For both the 2Fe/HMOR and 6Fe/HMOR catalysts (Fig. 4a), the stretching vibrational bands of the hydroxyl (OH) group are observed at 3794 cm^{-1} and 3662 cm^{-1}, corresponding to the presence of Si–OH and Al–OH groups, respectively.[44,45] Additionally, the band at 1647 cm^{-1} is indicative of water molecules adsorbed on the surface, revealing the presence of some moisture within the catalysts. Furthermore, absorption bands in the ranges of 1085 cm^{-1} and

Table 2 The surface area and pore volume properties determined by N_2-adsorption desorption isotherms compared with the Si/Al ratio and Fe content deduced from the SEM-EDS technique[a]

Samples	Surface area [$m^2\ g^{-1}$]	Microporous volume [$cm^3\ g^{-1}$]	Microporous area [$m^2\ g^{-1}$]	Mesopore volume [$cm^3\ g^{-1}$]	Mesopore area [$m^2\ g^{-1}$]	SEM-EDS	
						Si/Al	Fe (wt%)
HMOR	334	0.16	428	0.14	21.4	8.1	—
2Fe/HMOR	333	0.16	421	0.19	27.1	8.1	1.7
6Fe/HMOR	317	0.14	402	0.17	25.1	9.0	6.1
HZSM-5	239	0.11	273	0.04	54.8	12.5	—
2Fe/HZSM-5	195	0.03	237	0.18	27.8	15.6	1.7
6Fe/HZSM-5	143	0.02	170	0.14	21.3	12.7	5.6

[a] Calculation: surface area by BET, micropore volume and area by MP plot, and mesopore volume and area by BJH method.

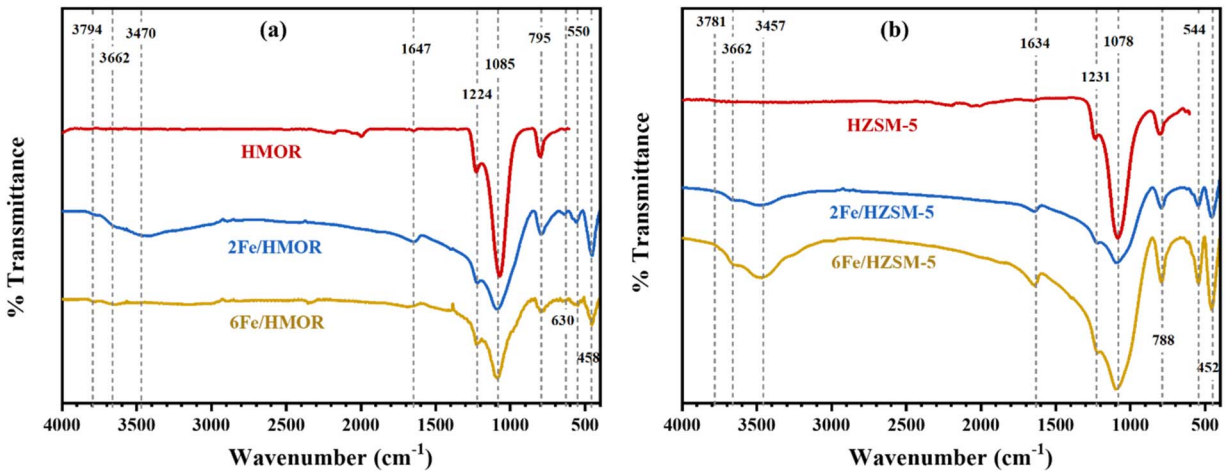

Fig. 4 FT-IR spectra of Fe/HMOR (a) and Fe/HZSM-5 (b) comparing with the bare zeolite supports.

795 cm^{-1} are associated with the asymmetric and symmetric stretching of the T–O–T bonds (where T represents Si or Al) within the zeolite framework. The bonds associated with framework zeolite structures were detected in both 2Fe/HZSM-5 and 6Fe/HZSM-5, as shown in Fig. 4b. Notably, the T–O–T bonds were observed at slightly lower wavenumbers, indicating weaker interactions within the zeolite framework. The presence of the Fe–O bond is represented by bands at 452 cm^{-1} and 544 cm^{-1}, which are linked to the formation of Fe clusters.[44,46]

3.1.5 Iron species on the Fe/zeolite catalysts

3.1.5.1 Bulk analysis by XANES. The X-ray absorption near edge structure (XANES) of Fe/HMOR and Fe/HZSM-5 is presented alongside reference spectra for Fe_2O_3 (hematite) and Fe_3O_4 (magnetite), as shown in Fig. 5a. The present iron oxide species play distinct roles in controlling these steps and the overall product selectivity through glucose conversion. The similarities in edge position and spectral shape suggest the coexistence of Fe^{3+} and mixed-valence Fe^{2+}/Fe^{3+} species within the catalysts, indicating a partial reduction of iron. These redox properties are significant because they can influence acidity and catalytic redox activity.

The relative proportions of Fe_2O_3 and Fe_3O_4 in the Fe/HMOR (Fig. 5b) and Fe/HZSM-5 (Fig. 5c) catalysts were quantified by linear combination fitting (LCF) of the Fe K-edge XANES spectra. For both zeolite supports, catalysts with Fe loadings between 1 and 4 wt% exhibit Fe_3O_4 as the predominant iron oxide species, indicating the stabilization of mixed-valence Fe^{2+}/Fe^{3+} states. Notably, Fe/HMOR shows a consistently higher Fe_3O_4 fraction than Fe_2O_3 across the investigated loading range, with the Fe_3O_4 contribution increasing progressively with Fe content. The maximum Fe_3O_4 fraction (~0.8) is observed for 6Fe/HMOR, evidencing a strong tendency toward partial reduction of iron species on the MOR framework.

In contrast, Fe/HZSM-5 catalysts display a more balanced distribution between Fe_3O_4 and Fe_2O_3. While 1Fe/HZSM-5 reaches a relatively high Fe_3O_4 fraction (~0.7), catalysts with 2–4 wt% Fe stabilize an average Fe_3O_4 fraction of ~0.6, implying a comparatively higher proportion of Fe_2O_3 (Fe^{3+}-rich species). These differences highlight the distinct influence of zeolite topology and metal–support interactions on iron redox chemistry. The larger one-dimensional channels and weaker confinement effects of MOR (0.6–0.7 nm in diameter) facilitate FeO*x* aggregation and enhance Fe–O–Fe connectivity, which favors the stabilization of mixed-valence Fe_3O_4-like species over fully oxidized Fe_2O_3. In contrast, the medium-pore MFI structure (0.52–0.57 nm in diameter) of ZSM-5 with a 3-dimensional pore structure, more effectively anchors isolated Fe^{3+} species to framework Al sites, thereby suppressing extensive reduction.[47]

The observed variation in iron oxide composition has important implications for catalysis. Fe_2O_3, composed

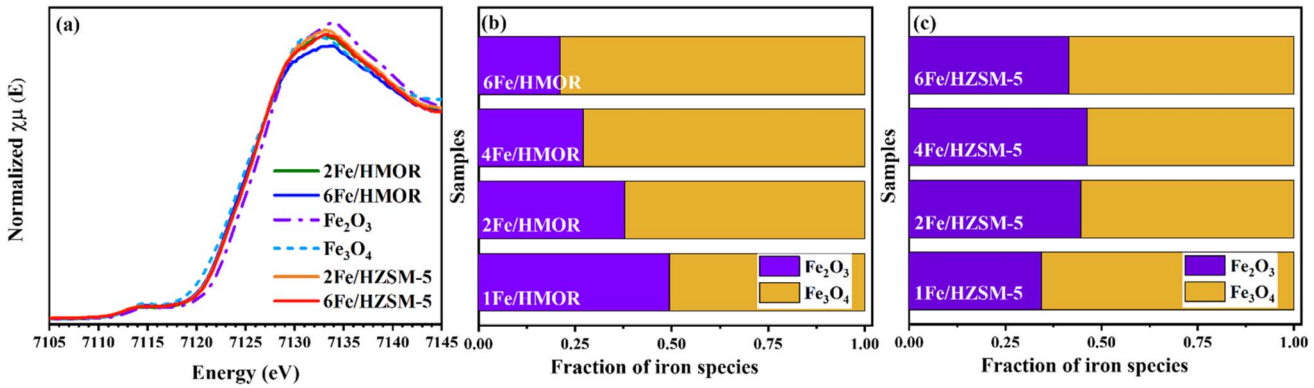

Fig. 5 XANES spectra of iron-supported catalysts compared with Fe_2O_3 and Fe_3O_4 (a), the fractions of Fe_2O_3 and Fe_3O_4 calculated using a linear combination fit of the XANES spectra for Fe/HMOR (b) and Fe/HZSM-5 (c).

predominantly of Fe^{3+} ions, provides strong Lewis acid sites that can promote glucose ring opening; however, their high electron-accepting character often leads to non-selective C–O bond cleavage and enhanced side reactions, resulting in reduced fructose selectivity.[17,48,49] Conversely, Fe_3O_4 contains mixed-valence Fe^{2+}/Fe^{3+} species that generate moderate Lewis acidity coupled with redox flexibility. This balanced acidity facilitates efficient and controlled glucose activation, minimizing excessive fragmentation and humin formation.

3.1.5.2 Surface analysis by XPS. An analysis of X-ray photoelectron spectroscopy (XPS) reveals the chemical environment of iron in Fe/HZSM-5 and Fe/HMOR by examining the core-level spectra of Fe 2p, Si 2p (or Si 1s), O 1s, and Al 2p, as reported in Fig. 6. These elements provide insights into the local

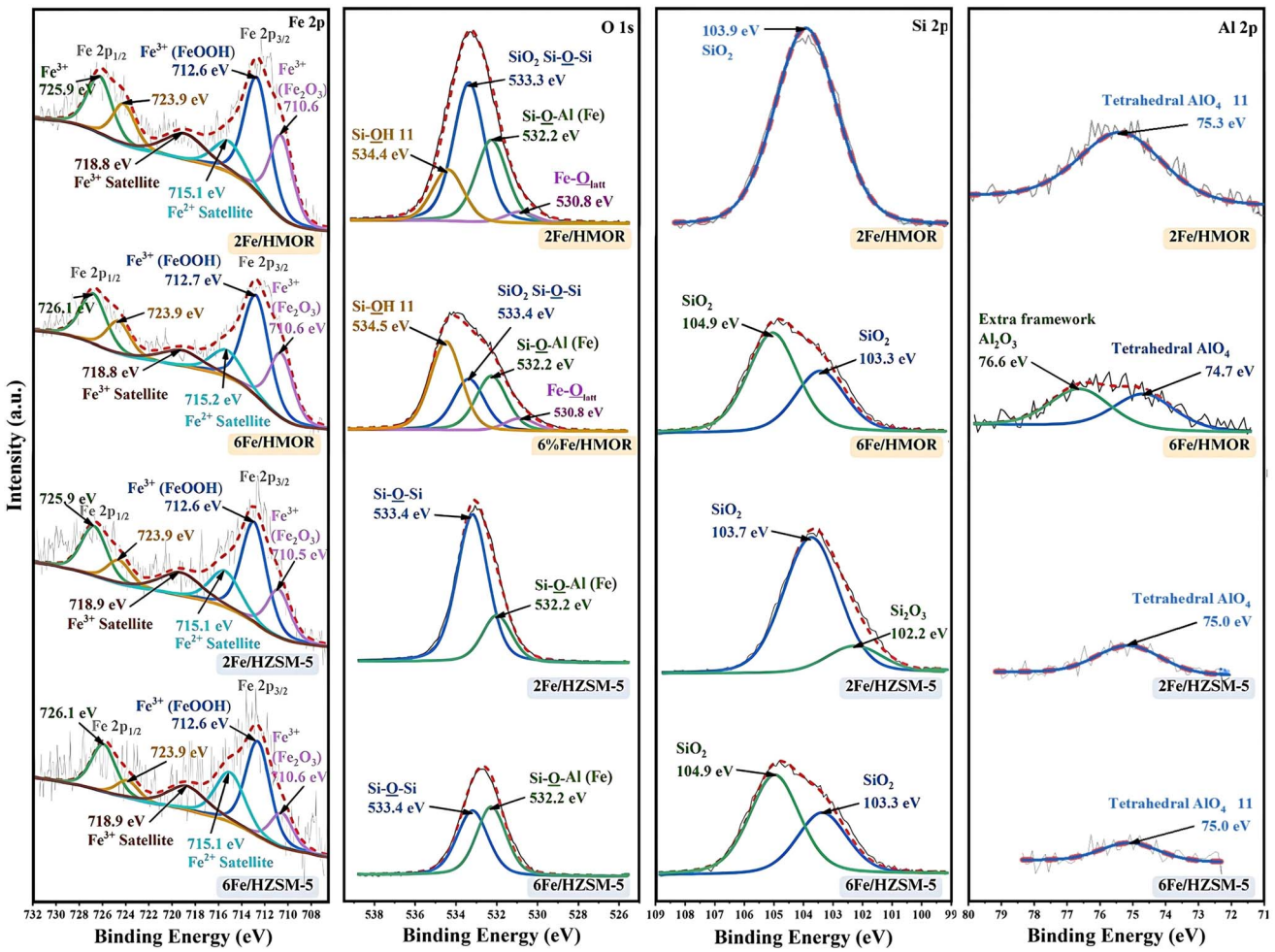

Fig. 6 XPS spectra of Fe 2p, O 1s, Si 2p, and Al 2p of Fe/HMOR and Fe/HZSM-5.

coordination of iron species and their interaction with the zeolite framework. The Fe $2p_{3/2}$ peak, which appears in the range of approximately 711–713 eV, confirms the presence of Fe^{3+} species in the forms of Fe_2O_3 and FeOOH on the surface.[50,51] The absence of satellite peaks typically associated with Fe^{2+} suggests that surface iron exists mainly as Fe_2O_3-like species or Fe^{3+} incorporated into the zeolite framework or extra-framework positions.[52] Moreover, these Fe^{3+} centers act as Lewis acid sites due to their electron-accepting nature, enabling coordination with oxygen-containing functional groups in glucose during the isomerization step.

The O 1s XPS spectra of the Fe/HMOR and Fe/HZSM-5 catalysts can be deconvoluted into distinct oxygen species that directly relate to the surface acid properties. The component at ~530 eV is attributed to lattice oxygen (O^{2-}) in Fe–O bonds of iron oxide species, which is associated with Fe^{3+} centers acting as Lewis acid sites. Peaks at ~532–533 eV correspond to framework oxygen in Si–O–Si and Si–O–Al(Fe) linkages,[53–55] reflecting the intact zeolite structure and the presence of framework Brønsted acid sites when Al is bonded to hydroxyl groups (Si–OH–Al). A higher-binding-energy component at ~534 eV is assigned to surface hydroxyl groups, including Si–OH, Fe–OH, and extra-framework Al–OH species, which function as Brønsted acid sites capable of proton donation. The relative intensity of these hydroxyl-related O 1s signals increases upon Fe loading, indicating that iron incorporation introduces additional metal-associated Brønsted acidity while simultaneously generating Fe-based Lewis acid sites. This coexistence of lattice oxygen-associated Lewis sites and hydroxyl-derived Brønsted sites on the catalyst surface provides a clear explanation for the bifunctional acid behavior observed in glucose conversion to 5-HMF.

The Si 2p peak at 103–104 eV observed for all catalysts confirms the presence of framework SiO_2,[56,57] indicating that the zeolite structure is largely preserved after iron incorporation. However, the shift of the Si 2p signal to ~105 eV for the 6Fe/HMOR and 6Fe/HZSM-5 catalysts suggests the formation of amorphous SiO_2,[52,55] reflecting partial framework deconstruction at high Fe loadings. The Al 2p spectra further reveal that while most catalysts retain framework AlO_4^- species (74–75 eV), the 6Fe/HMOR catalyst exhibits an additional Al 2p component at ~76 eV, assigned to extra-framework Al_2O_3,[58,59] consistent with partial dealumination and SEM-EDS observations (Fig. 3b). This structural modification implies that Fe^{3+} species partially replace protons at framework Al sites, modifying the original Brønsted acid sites. In parallel, the Fe 2p spectra confirm the predominance of surface Fe^{3+} species, which act as Lewis acid sites, while O 1 s deconvolution identifies Fe–O lattice oxygen

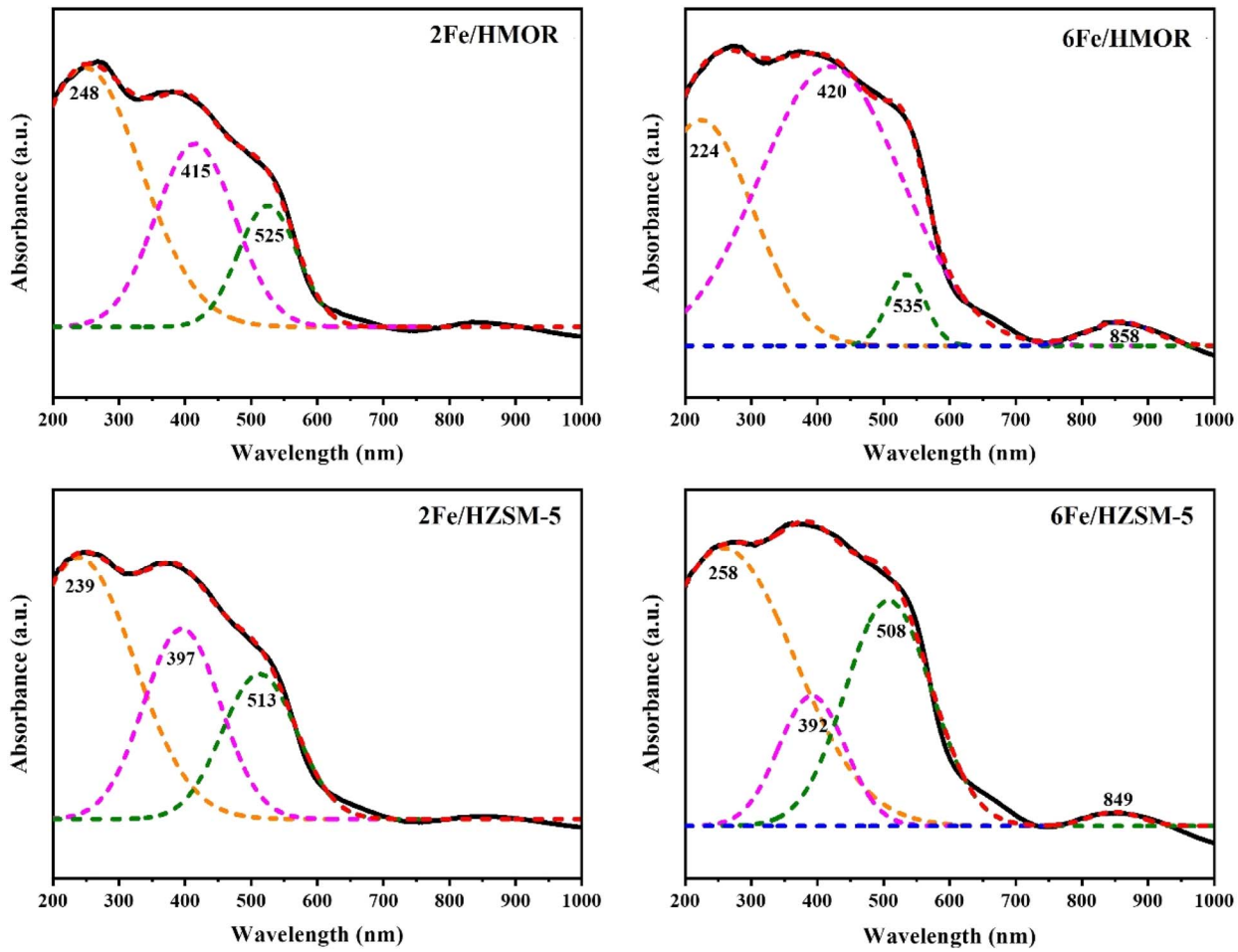

Fig. 7 UV-vis spectra of the Fe/HMOR and Fe/HZSM-5 catalysts.

(Lewis acid-related) and surface hydroxyl groups (Si–OH, Fe–OH, Al–OH) that function as Brønsted acid sites. Together, these results indicate that high Fe loading leads to a surface composed of framework SiO_2, isolated and clustered Fe^{3+} species, Fe–O and Fe–OH groups, and extra-framework Al_2O_3, creating a mixed Lewis–Brønsted acidic surface. This coexistence of iron- and aluminum-derived acid sites provides a rational explanation for the enhanced catalytic activity and selectivity toward 5-HMF formation observed for the Fe-supported zeolite catalysts.

3.1.5.3 Distribution of the iron species on zeolites by UV-vis DRS. UV-vis Diffuse Reflectance Spectroscopy (UV-vis DRS) is a crucial technique for investigating the electronic environment of metal species. The deconvoluted UV-vis results presented in Fig. 7 offer quantitative information regarding the distribution of various iron species, as expressed in Table 1. Four primary absorption regions were identified: isolated Fe^{3+} in tetrahedral and octahedral coordination (λ < 300 nm), oligomeric Fe_xO_y clusters (λ = 300–450 nm), small iron oxide particles (λ = 450–600 nm), and large iron oxide particles (λ > 600 nm).[11] The 2Fe/HMOR catalyst primarily contains isolated Fe^{3+} species, which make up 57% of its composition. It also has significant amounts of oligomeric clusters (29%) and small particles (14%). In comparison, the 6Fe/HMOR catalyst shows a noticeable increase in oligomeric clusters, comprising 59%, while the proportion of isolated Fe^{3+} species decreases to 35%. In the HZSM-5 series, the 2Fe/HZSM-5 sample shows a distribution comparable to that of the 2Fe/HMOR. However, the 6Fe/HZSM-5 sample displays a higher percentage of isolated Fe^{3+} (58%) compared to the HMOR sample. Additionally, the 6Fe/HZSM-5 sample reveals an increased formation of small particles (28%) instead of oligomeric clusters. The differences in iron speciation highlight how zeolite composition and structure affect the stabilization of various iron species. The broader channels and higher aluminum content of HMOR enhance the formation of oligomeric iron clusters at higher loadings. Meanwhile, the more restricted pore system of HZSM-5 encourages the development of surface iron oxide nanoparticles.

3.1.6 Acidity by ammonia temperature programmed desorption (NH_3-TPD). The NH_3-TPD profiles revealed significant differences in the acid properties of the catalysts, as shown in Fig. 8. Total acidity indicates the amount of compensated H^+ ions on the catalyst surfaces, comprising weak (100–250 °C), medium (250–450 °C), and strong (450–600 °C) acid sites.[60] The weak acidic range is associated with physisorbed NH_3 molecules on Si–OH groups of zeolites. In contrast, the medium- and strong-acid sites relate to chemically adsorbed NH_3 on hydroxyl groups (–OH) associated with Al sites.[59] The HMOR zeolite exhibited a total acidity of approximately 120 μmol g^{-1}, consisting of weak (49.6 μmol g^{-1}), medium (13.0 μmol g^{-1}), and strong acid sites (57.4 μmol g^{-1}), as summarized in Table 3. The presence of highly acidic sites indicates strong chemisorption of NH_3 on hydroxyl-bound Al sites within the HMOR zeolite. In comparison, the total acidity of HZSM-5 was approximately 80 μmol g^{-1}, which is lower than that of HMOR. Additionally, strong acid sites were not identified in HZSM-5. After iron modification, the total acidity of Fe/HMOR decreased,

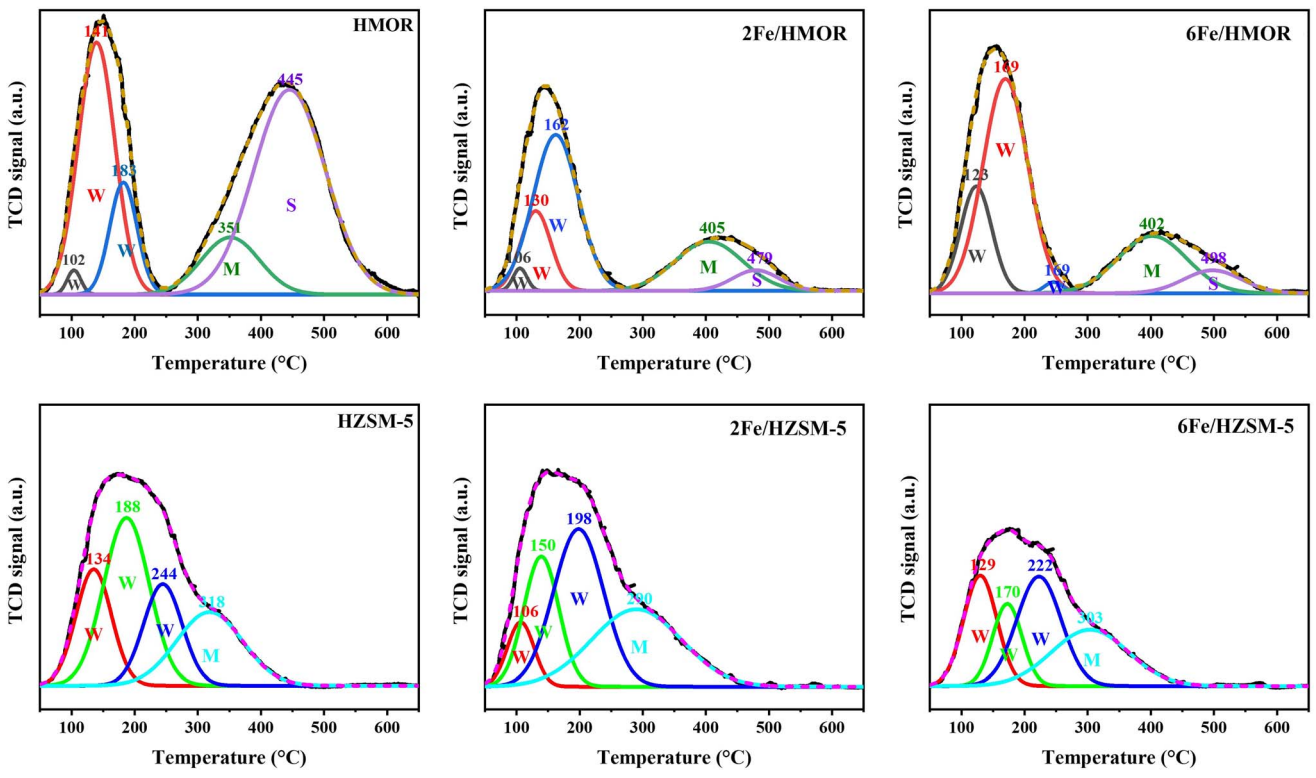

Fig. 8 NH_3-TPD profiles of the Fe/HMOR and Fe/HZSM-5 catalysts compared with the bare zeolites.

accompanied by a significant decline in the number of strong acid sites. These results suggest the ion exchange of Fe^{3+} ions with –OH groups bound to the Al sites of the zeolite. For Fe/HZSM-5, the total acidity decreased with increasing Fe loading to 6 wt%. Notably, the medium acid site in 2Fe/HZSM-5 increased significantly compared to bare HZSM-5. Furthermore, the desorption temperature shown in Fig. 8e shifted slightly to a lower energy. This change can be attributed to an increase in chemisorbed NH_3 species associated with –OH groups bound to oligomeric Fe_xO_y and clusters dispersed on the zeolite surface, as determined by the UV-vis DRS analysis.

NH_3-TPD was used to quantify the total acidity and acid strength distribution of the catalysts, but cannot distinguish between Brønsted and Lewis acid sites, as NH_3 adsorbs non-selectively on both. The parent HMOR exhibits higher total acidity and a larger fraction of strong acid sites than HZSM-5, which can promote side reactions during glucose conversion. After Fe modification, the total acidity, particularly strong acid sites, decreases, indicating partial ion exchange of Fe^{3+} with framework Al–OH groups, as suggested by the XPS result, and a moderation of acidity. In Fe/HZSM-5, the increase in medium-strength acid sites at low Fe loading reflects the formation of accessible acidic centers associated with dispersed Fe species.

3.1.7 Diffuse reflectance infrared Fourier transform spectroscopy (DRIFTS) of adsorbed pyridine (Py-IR). Pyridine adsorption, as illustrated in Fig. 9, was employed to evaluate the alterations in various types of acid sites. Typically, the pyridine adsorption bands observed at approximately 1445 cm^{-1} and 1545 cm^{-1} are attributed to pyridine coordinated with Brønsted (B) and Lewis (L) acid sites, respectively.[61] The total acidity of the catalysts declines with increasing Fe loading. The B/L ratios calculated from the peak areas of the Py-IR spectra are also presented in Table 3. The introduction of Fe through impregnation on HZSM-5 and HMOR resulted in increased B/L ratios. An increase in the B/L ratio signifies a rise in Brønsted acids or a reduction in Lewis acid sites. The specific characteristics and dispersion of the iron species[61] influence the Lewis acidity of the Fe-loaded catalyst. The observed decrease in Lewis acid sites may be attributed to surface and pore blocking of the zeolite crystalline structure by oligomeric, clustered, or smaller particles of the iron species, as determined by UV-vis DRS (in Table 1). A notable increase in the B/L ratio in Fe/HMOR correlates well with a high concentration of oligomeric iron species. Additionally, the presence of monomeric and oligomeric ferric ions, such as $[Fe(OH)_2]^+$ and $[HO–Fe–O–Fe–OH]^{2+}$ in their hydrated forms, acts as a Brønsted acid site. Upon dehydration, these species are expected to convert to $[FeO]^+$ and $[–Fe–O–Fe–]^{2+}$ in their dehydrated forms.[62] Meanwhile, the modest increase in the B/L ratio for Fe/HZSM-5 is associated with a higher iron oxide cluster content.

The Py-IR results are crucial for assessing the relative contributions of Lewis acid sites in the initial reaction phase, specifically the isomerization of glucose to fructose. While Lewis acid sites typically play a key role in this process, the current findings suggest that the highly dispersed monomeric and oligomeric Fe species in Fe/HMOR can generate Brønsted acidity through hydrated Fe–OH species, which work synergistically with the remaining Lewis sites. This phenomenon accounts for the higher B/L ratio observed in Fe/HMOR, while still preserving its effective catalytic activity. In contrast, the more modest increase in the B/L ratio for Fe/HZSM-5 aligns with the presence of a greater proportion of iron oxide clusters, which contribute less effectively to the catalysis.

3.1.7.1 Fe species and acid-site balance on glucose conversion to 5-HMF. The combined characterization results reveal that the nature and balance of Brønsted and Lewis acid sites strongly depend on the zeolite support and iron speciation, which together govern glucose conversion to 5-HMF. HMOR-supported catalysts favor the formation of oligomeric and hydrated Fe species, as evidenced by UV-vis DRS and XANES, facilitated by the larger pore structure and higher aluminum content of HMOR. These species generate both Lewis acid sites (Fe^{3+} centers) and additional Brønsted acid sites (Fe–OH and extra-framework Al–OH), as confirmed by XPS (Fe 2p and O 1s) and reflected in the significantly increased B/L ratio observed by Py-IR. In contrast, HZSM-5 stabilizes a higher fraction of isolated Fe^{3+} and iron oxide clusters, leading to a more modest increase in the B/L ratio, as Lewis acidity remains relatively dominant. Although NH_3-TPD shows that total acidity decreases after Fe incorporation for both supports, this technique cannot distinguish acid types; Py-IR clearly demonstrates that Fe/HMOR exhibits a Brønsted-enriched acidic surface, while Fe/HZSM-5 retains a more Lewis-acid-dominated character. Mechanistically, Lewis acid sites (Fe^{3+}) promote glucose activation and isomerization to fructose, whereas Brønsted acid sites (Si–OH–Al, Fe–OH, and Al–OH) drive the subsequent dehydration of fructose to 5-HMF. The higher B/L ratio in Fe/HMOR therefore reflects a more effective bifunctional acid system, enabling controlled isomerization–dehydration synergy and improved 5-HMF formation, while excessive Lewis acidity

Table 3 Total acidity and distribution of the acid density in weak, medium, and strong sites regarding desorption temperature in NH_3-TPD profiles and the ratio of Brønsted and Lewis (B/L) acid sites integrated from Py-IR spectra

Samples	Total acidity [μM]	Weak [μM] (100–250 °C)	Medium [μM] (250–450 °C)	Strong [μM] (450–600 °C)	B/L ratio by Py-IR
HMOR	120.3	49.6	13.0	57.7	0.2
2Fe/HMOR	55.1	38.3	13.1	3.8	1.3
6Fe/HMOR	72.3	38.3	15.5	5.2	1.6
HZSM-5	80.5	61.5	19.0	—	0.4
2Fe/HZSM-5	82.7	55.5	27.2	—	0.7
6Fe/HZSM-5	59.6	42.8	16.8	—	1.0

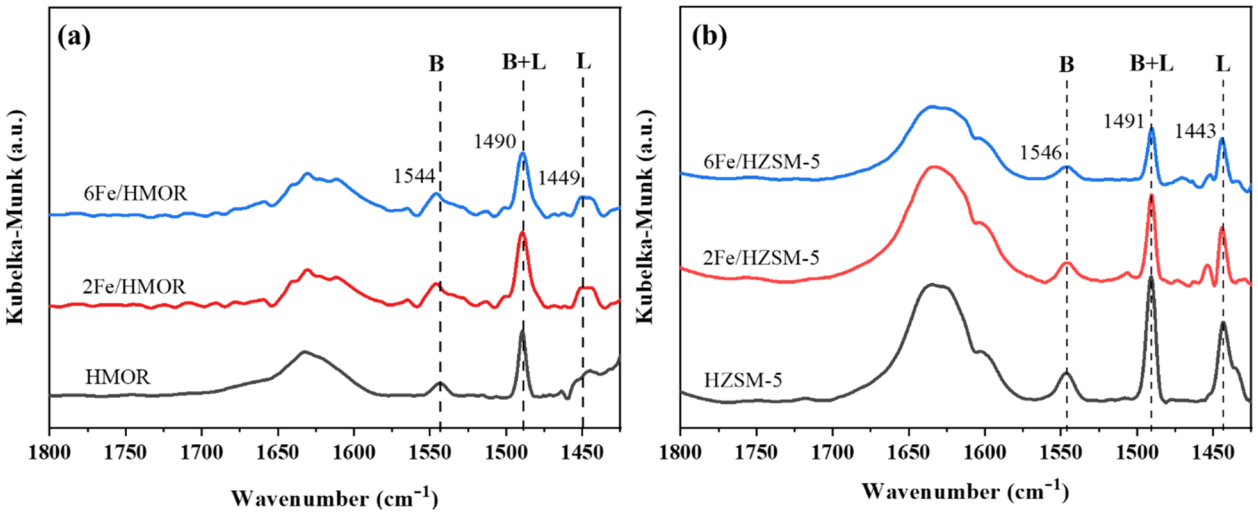

Fig. 9 Py-IR of the Fe/HMOR (a) and Fe/HZSM-5 (b) catalysts compared with the bare zeolites.

or strong Brønsted acidity can lead to side reactions. This analysis demonstrates that tuning the B/L ratio through support selection and iron speciation is critical for optimizing glucose-to-5-HMF conversion.

The structural differences between Fe/HMOR and Fe/HZSM-5 lead to variations in how iron oxide (FeO*x*) behaves and in its acidity. Analyses show that Fe/HMOR mostly has larger FeO*x* clusters with more Fe_3O_4, while Fe/HZSM-5 has more isolated Fe_2O_3. The use of pyridine-IR indicates that Fe/HMOR has a higher ratio of Brønsted to Lewis acid sites, due to the combination of framework Brønsted sites and Fe–OH acidity. In contrast, Fe/HZSM-5 has stronger Lewis acidity. These differences might affect how well they work in chemical reactions. The balanced acidity and Fe_3O_4 in Fe/HMOR promote glucose isomerization and the selective conversion to 5-HMF. In comparison, the confined structure of Fe/HZSM-5 promotes unwanted side reactions due to its high Lewis acidity. This comparison shows that the structure of zeolites is crucial in shaping how iron species form and how acid sites interact, ultimately affecting the selectivity for 5-HMF.

Although Al- and Si-derived acid sites inherently participate in glucose conversion, their influence on product selectivity in this study is deliberately controlled and secondary. All catalysts were prepared from parent HMOR and HZSM-5 zeolites with fixed Si/Al ratios, and Fe was introduced *via* mild impregnation, minimizing the generation of extra-framework Al species that could increase Brønsted acidity. Pyridine-IR results show that Fe incorporation predominantly introduces Fe-based Lewis acid sites while leaving the framework Brønsted acidity (Si–OH–Al) largely unchanged. Consistently, NH_3-TPD indicates that Fe loading mainly modifies acid strength distribution rather than total acidity. If Al or Si residues were the dominant factor, comparable 5-HMF selectivity would be expected for catalysts with similar Si/Al ratios; however, Fe/HMOR exhibits markedly higher selectivity than Fe/HZSM-5. Furthermore, spectroscopic analysis reveals a strong correlation between 5-HMF selectivity

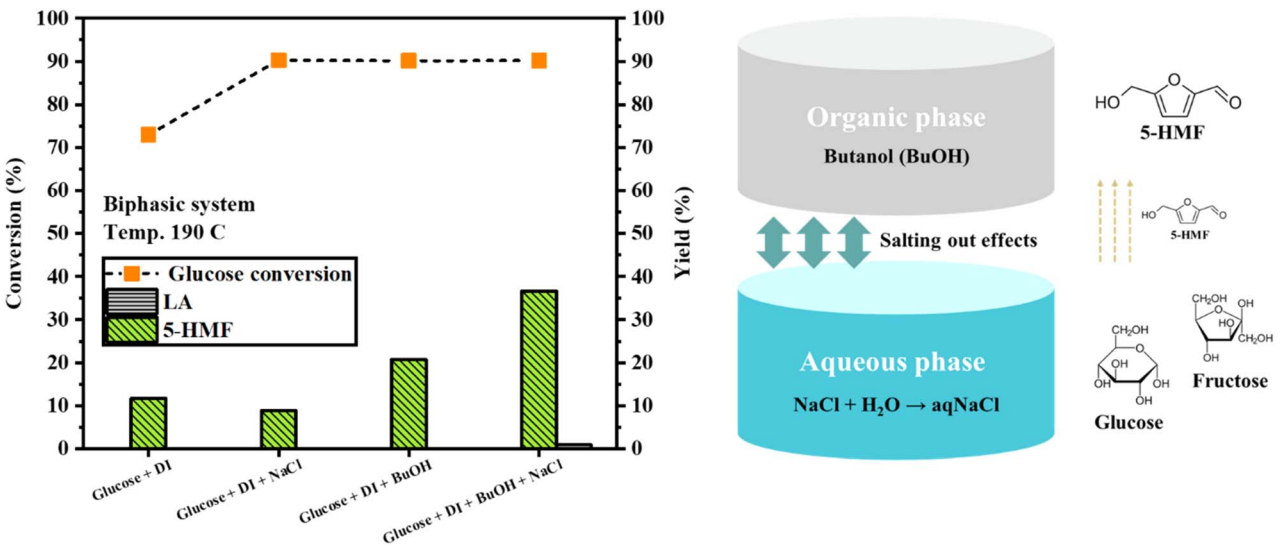

Fig. 10 Glucose conversion in water and *n*-butanol/water media systems of 6Fe/HMOR.

and the fraction of Fe_3O_4 species, which provides an optimized Brønsted/Lewis acid balance that promotes glucose isomerization and dehydration while suppressing Brønsted-acid-driven side reactions. These results demonstrate that Fe speciation and its interaction with zeolite topology, rather than Al or Si residues alone, govern the observed selectivity enhancement.

3.2 Catalytic performance for glucose conversion

3.2.1 Catalytic enhancement in a biphasic system. The impact of employing a biphasic system of *n*-butanol (*n*-BuOH) and water, as opposed to using pure water, was evaluated with HMOR catalysts, as shown in Fig. 10. The results demonstrated that the catalytic conversion of glucose and the selectivity for 5-HMF in the biphasic system were significantly enhanced compared to the water-only system. However, LA production *via* the hydration mechanism was hindered in both systems. Additionally, introducing NaCl into the system increased the selectivity for 5-HMF by raising the ionic strength of the aqueous phase through ion–dipole interactions between Na^+ and Cl^- ions and water,[63] as illustrated in the reaction scheme in Fig. 10. This increase in ionic strength reduced the solubility of 5-HMF in the aqueous phase, thereby preventing its further degradation into LA. This change also facilitated the removal of 5-HMF, shifting the reaction equilibrium toward its formation.

Moreover, the biphasic system enhances mass transfer, enabling glucose and its intermediates to diffuse more readily between the aqueous and organic phases. The organic phase provides a protective environment for 5-HMF, partially shielding it from the acidic conditions in the aqueous phase, which are conducive to LA formation. As a result, the biphasic system proves to be more effective in converting glucose and producing 5-HMF compared to the monophasic system.

3.2.2 Effect of temperature. The effect of temperature on glucose conversion and product yields was studied using 6Fe/HMOR and 6Fe/HZSM-5, comparing these catalysts with bare zeolites in a biphasic reaction system, as shown in Fig. 11. The results indicated that both glucose conversion and the yield of 5-HMF increased with temperature, reaching up to 200 °C. At temperatures of 190 °C and 200 °C, the catalytic conversion and yield of 5-HMF for 6Fe/HMOR and 6Fe/HZSM-5 were significantly better than those of the bare zeolites. This demonstrates that incorporating iron onto zeolites HMOR and HZSM-5 enhances catalytic performance in the conversion of glucose to 5-HMF. Moreover, the byproduct of LA over 6Fe/HMOR and 6Fe/HZSM-5 was lower than that over the bare zeolite. The 6Fe/HMOR catalyst achieved the highest yield of 5-HMF at 200 °C, which was nearly the same as the yield obtained at 190 °C. In contrast, the optimal yield for 6Fe/HZSM-5 occurred at 190 °C. Therefore, to minimize energy consumption, a reaction temperature of 190 °C is recommended for further studies.

3.2.3 Effect of Fe loading. The effect of iron loading on catalytic performance was evaluated under optimized reaction conditions, as summarized in Table 4. In the HMOR series, an

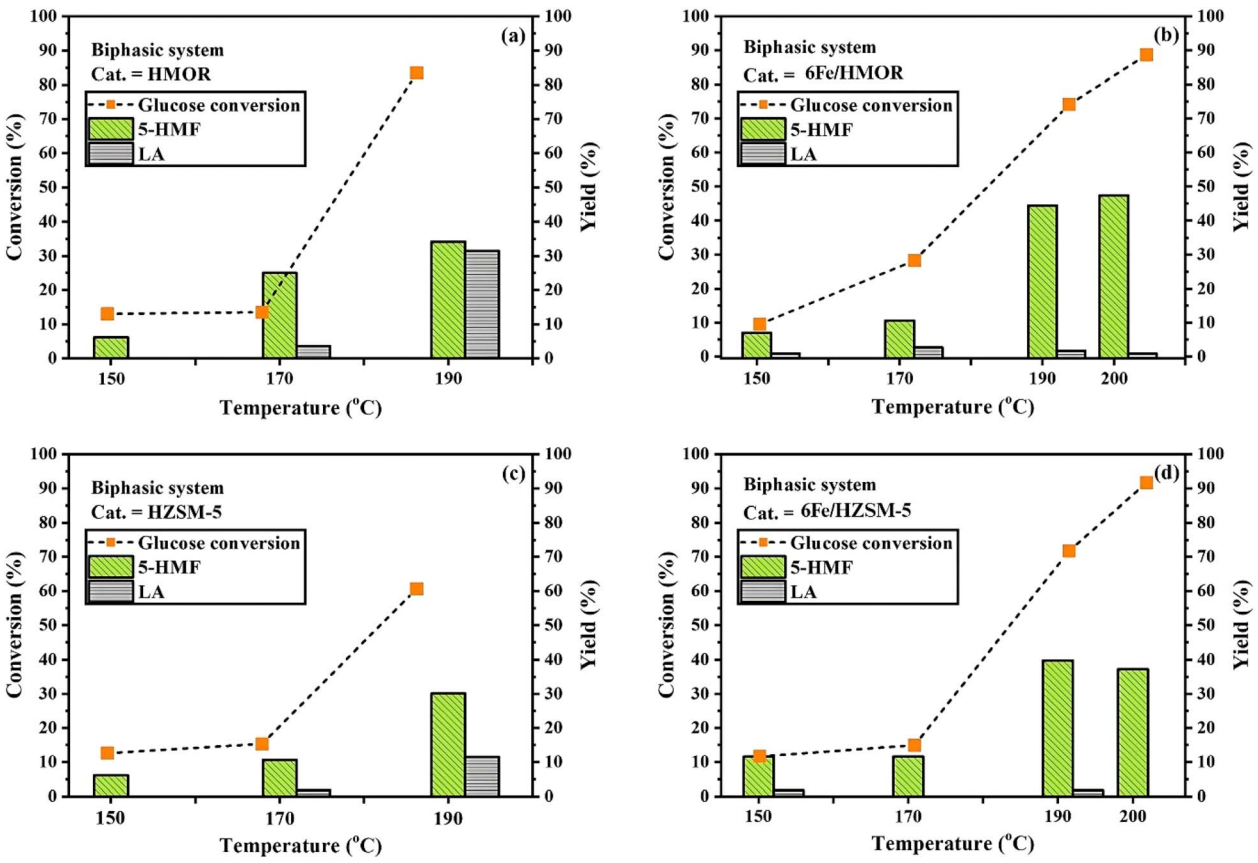

Fig. 11 Temperature effect on glucose conversion of HMOR (a), 6Fe/HMOR (b), HZSM-5 (c), and 6Fe/HZSM-5 (d).

Table 4 The catalytic conversion of glucose for Fe/HMOR and Fe/HZSM-5 with different Fe-loading in a biphasic system at 190 °C for 4 h

Catalysts	% Conversion	% Yield of 5-HMF	% Yield of LA
HMOR	90	34	31
2Fe/HMOR	87	36	14
6Fe/HMOR	79	44	2
HZSM-5	63	30	12
2Fe/HZSM-5	61	36	0
6Fe/HZSM-5	76	40	2

increase in iron content was associated with a rise in the yield of 5-HMF from glucose. However, the glucose conversion percentage did not increase gradually with increasing Fe loading. This finding reveals the effects of metal dispersion on the zeolite support. Reduction in glucose conversion due to lower accessibility or weaker acid strength is presented on the zeolite support. When Fe species are highly dispersed in zeolite (as isolated Fe^{3+} or Fe–O–Si sites), they may be confined deep inside micropores or strongly bonded to the framework. The present active species well corresponded to a finding of extra-framework Al_2O_3 by XPS analysis on the catalyst. Conversely, for the HZSM-5 series, glucose conversion improved with increasing Fe content. These findings align well with the specific surface area of the catalysts. The yields of iron-supported catalysts on both zeolites were enhanced with greater Fe loading. The maximum yields were observed for the 6Fe/HMOR and 6Fe/HZSM-5 catalysts, reaching approximately 44% and 40%, respectively. However, LA production decreased as Fe loading increased.

The physicochemical properties of the catalysts were thoroughly characterized, as they are linked to their catalytic activity and selectivity for the identified products. The yields of 5-HMF and LA were normalized by surface area, as shown in Fig. 12. The normalized yields of the identified products increased with increasing iron (Fe) loading for both HMOR and HZSM-5 supports. Notably, significant improvements in yield were particularly evident with the Fe/HZSM-5 catalysts, with the highest yield achieved using the 6Fe/HZSM-5 catalyst. Additionally, both the 6Fe/HMOR and 6Fe/HZSM-5 catalysts exhibited a reduction in LA byproduct compared to the bare zeolites. Regarding the ratio of weak to medium acid sites (W/

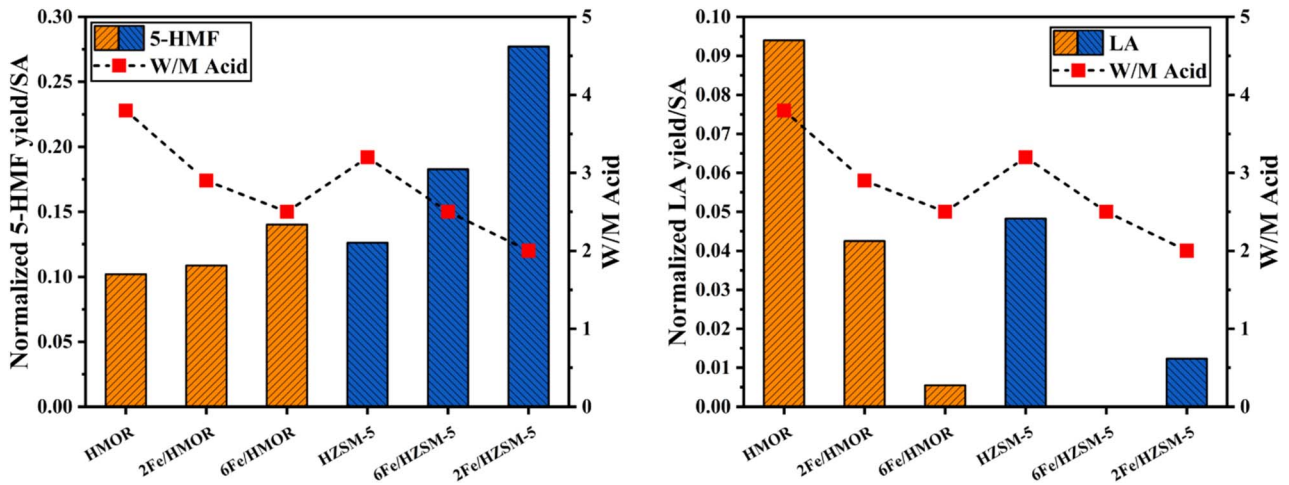

Fig. 12 Relationship of the normalized product yields of 5-HMF and LA with a weak to medium (W/M) acid ratio of the catalysts on glucose conversion under a biphasic system at 190 °C.

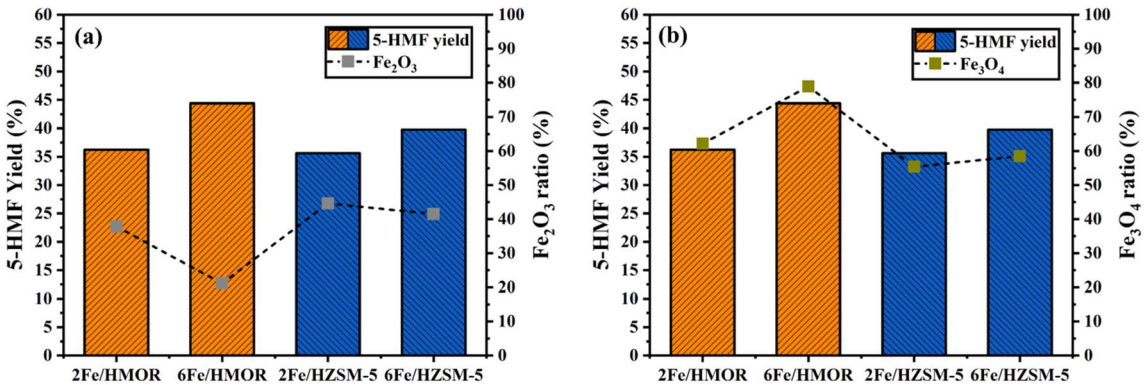

Fig. 13 Relationship of 5-HMF yield and Fe_2O_3 (a) and Fe_3O_4 (b) on Fe/HMOR and Fe/HZSM-5 catalysts in glucose conversion under a biphasic system at 190 °C.

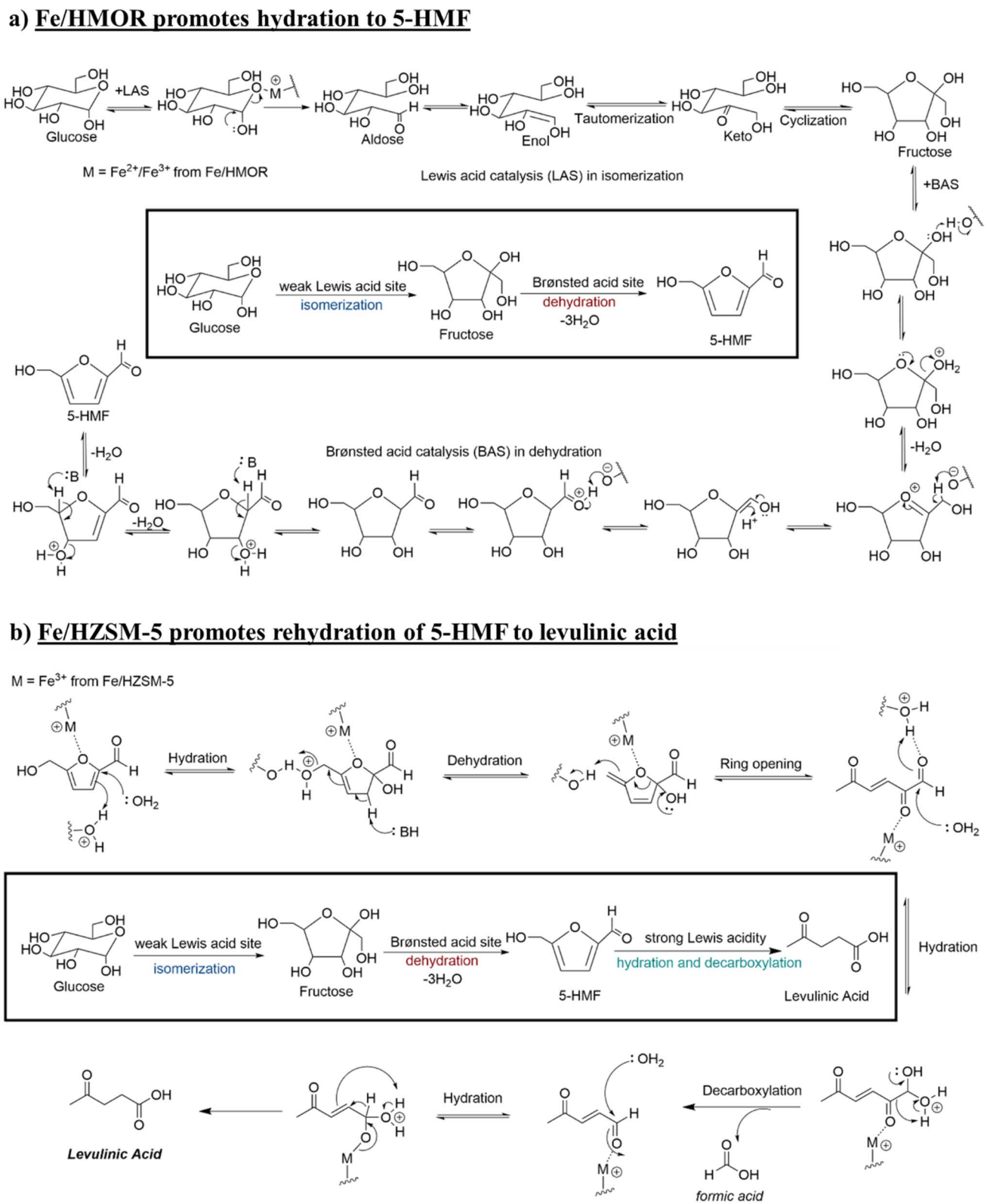

Fig. 14 Reaction mechanism of glucose conversion to 5-HMF (a) and levulinic acid (b) catalyzed by Lewis acid site (LAS) and Brønsted acid site (BAS).

M), analyzed by HN_3-TPD, the distribution of 5-HMF products increased as the W/M ratio decreased. Conversely, the production of LA increased with a higher W/M ratio (Fig. 12). This indicates that achieving a balance between weak acid sites (Si–OH) and medium acid sites, which correspond to the hydroxyl groups bound to Fe and Al within the zeolite structures, plays

a crucial role in product selectivity during glucose conversion. These findings are essential for optimizing catalysts in iron-supported zeolites.[17,19,64]

3.2.4 Effect of Fe species on 5-HMF selectivity. The distribution of Fe_2O_3 and Fe_3O_4 in iron-supported zeolite catalysts was analyzed using Linear Combination Fitting (LCF) of X-ray Absorption Spectroscopy (XAS) spectra. The results were plotted alongside the yield of 5-HMF for the catalysts, as shown in Fig. 13(a) and (b). A strong correlation was observed between the presence of Fe_3O_4 species, which contain both Fe^{2+} and Fe^{3+} ions, in the Fe/HMOR and Fe/HZSM-5 catalysts and the yield of 5-HMF. In the 6Fe/HMOR catalyst, the maximum yield reached approximately 45%, with the fraction of Fe_3O_4 around 76% (see Fig. 13b). In contrast, catalysts with a higher proportion of Fe_2O_3, which primarily consists of Fe^{3+}, displayed a lower yield of 5-HMF. This lower yield can be attributed to the stronger acidic character of Fe_2O_3 nanoparticles compared to Fe_3O_4, which serves as the Lewis acid site in the catalysts. This difference creates a more favorable reaction pathway for the hydration process of 5-HMF, leading to the production of LA.

The proposed reaction mechanism for glucose conversion considers the roles of both Brønsted and Lewis acid sites in the catalysts, as illustrated in Fig. 14.[64] The glucose is first subjected to Lewis acid catalysis. The heteroatom oxygen forms ionic contact with the metal, facilitating aldehyde formation from the alcohol by breaking the carbon-oxygen sigma bond. With the ring broken, the aldose can undergo keto–enol tautomerization to form the keto form, featuring a ketone. Cyclization generates fructose. Fructose can undergo dehydration at a Brønsted acid site, where three water molecules are lost. Initially, the anomeric alcohol undergoes protonation, and the formation of an oxocarbenium from the heteroatom oxygen facilitates water removal. The removal of the acidic proton forms the enol, and the deprotonated Brønsted acid catalyst deprotonates the proton from the newly made oxonium ion. The removal of the second water molecule occurs when the base removes the acidic proton on the alpha carbon of the aldehyde, and the water is eliminated. The final water molecule is removed by base elimination, with the driving force being the formation of a stable five-membered aromatic 5-HMF. Both Fe_3O_4 and Fe_2O_3 predominantly act as Lewis acid sites involved in the isomerization of glucose to fructose. However, the surface of these iron oxides contains –OH groups that are relevant to Brønsted acid sites, as confirmed by XPS.[65] Thus, the Fe–OH and Si–OH groups on the Fe/zeolite catalysts play a role in catalyzing the conversion of fructose to 5-HMF. Moreover, the size of the Fe_3O_4 clusters significantly influences the pathway that determines the yield of 5-HMF by modulating the strength of the Brønsted acid sites on Fe_3O_4/SiO_2, as reported in the literature.[66] A larger size of the iron oxide cluster found in the 6Fe/HMOR, as determined by SEM-EDS, shows a higher yield of 5-HMF compared to the 6Fe/HZSM-5 catalyst. Additionally, the presence of extra-framework Al_2O_3 on the surface of the 6Fe/HMOR catalyst, as determined by XPS, also influences the selectivity of the 5-HMF product. This finding has been documented in the literature.[59,64] The relatively high amount of strongly acidic sites, combined with the mixed acidic nature of Lewis and Brønsted acid sites, can effectively tune the conversion of glucose to 5-HMF.

The mechanistic scheme (Fig. 14) also illustrates the explicit influence of acid-site distribution and Fe-speciation on the parallel formation pathways of 5-HMF and levulinic acid. Mixed-valence Fe_3O_4 species provide moderate Lewis acidity that promotes selective glucose isomerization, while the Brønsted Fe–OH and Si–OH groups catalyze fructose dehydration to 5-HMF. A lower weak-to-medium acidity (W/M) ratio, characteristic of Fe/HMOR, favors dehydration and suppresses rehydration of 5-HMF. On the other hand, catalysts with higher proportions of Fe_2O_3 and higher W/M ratios, such as Fe/HZSM-5, display stronger Lewis acidity which can promote and accelerate the reaction of 5-HMF rehydration to levulinic acid. This explains why Fe/HMOR and Fe/HZSM-5 exhibit comparable glucose conversion and 5-HMF yield yet differ markedly in levulinic acid formation.

Although the 5-HMF yield (44%) is lower than reported in some recent studies, this study provides detailed insights into the synergistic roles of Fe species and the acid site balance, which are crucial for designing improved catalysts for future studies.

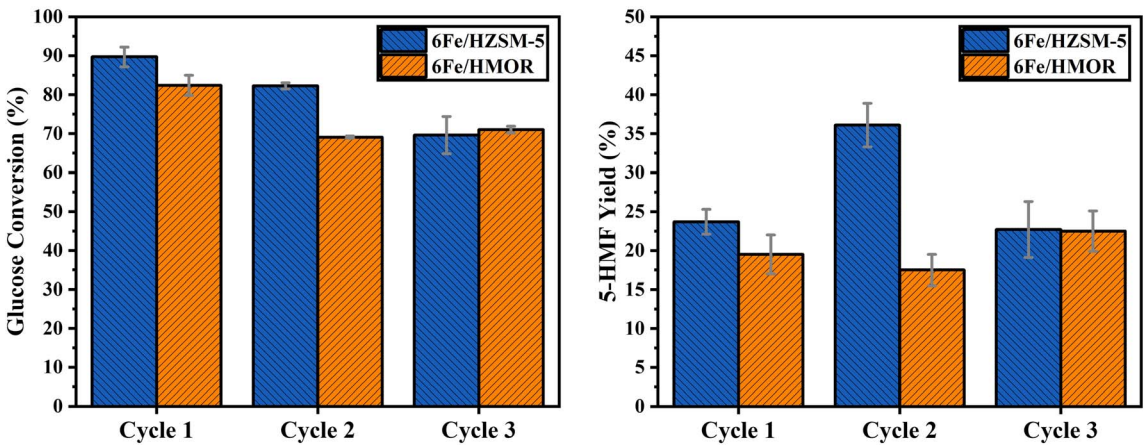

Fig. 15 Glucose conversion and 5-HMF yield over three catalytic cycles. Each cycle was performed in triplicate.

3.2.5 Reusability of 6Fe/HZSM-5 and 6Fe/HMOR. The reusability of the 6Fe/HZSM-5 and 6Fe/HMOR catalysts was evaluated at 190 °C over a period of 4 h in a biphasic solvent system, as illustrated in Fig. 15. The catalytic conversion and 5-HMF yield from the 6Fe/HZSM-5 catalyst were slightly higher than those from the 6Fe/HMOR catalyst across three running

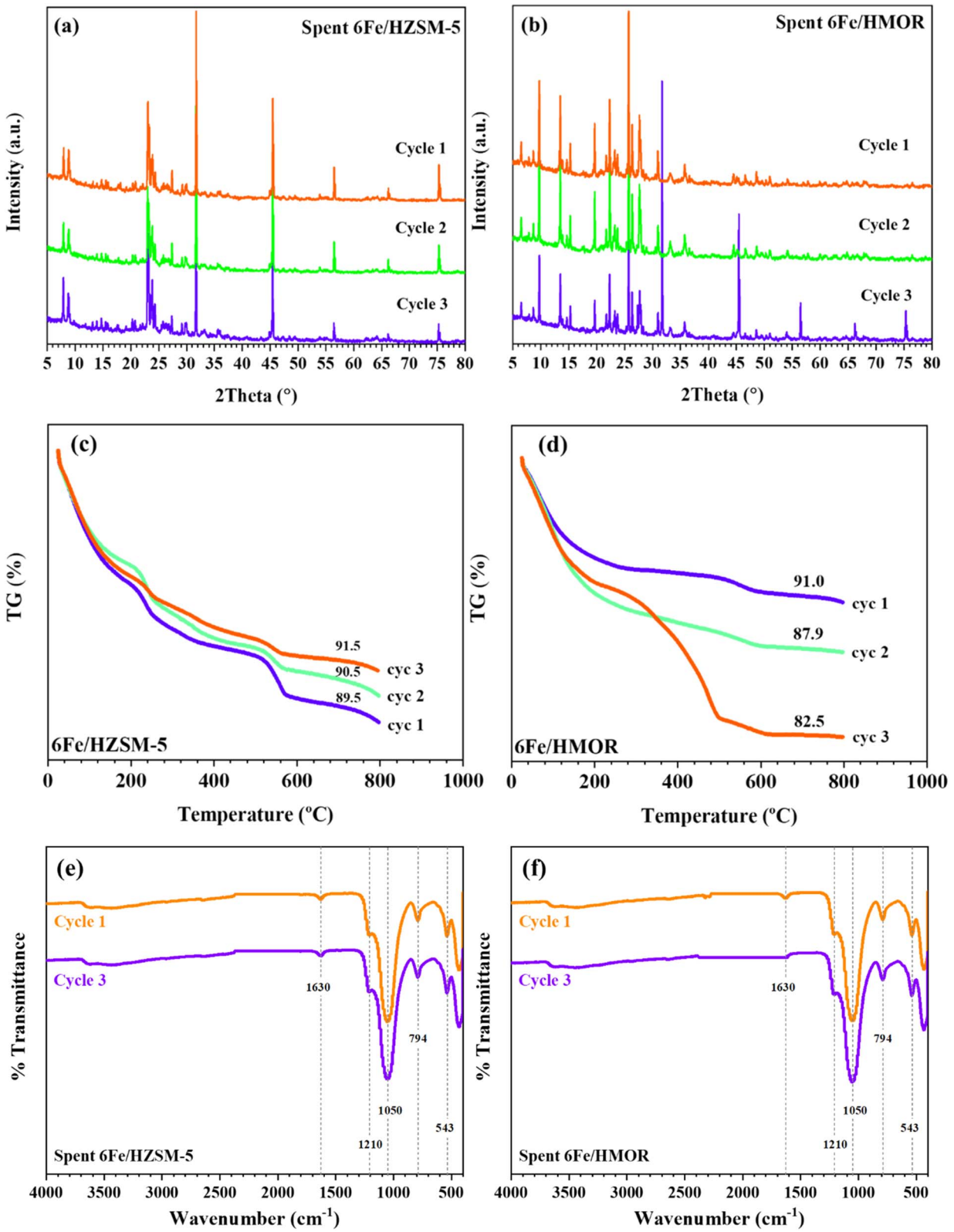

Fig. 16 XRD patterns (a and b), TGA analysis (c and d), and FTIR spectra (e and f) of the spent catalysts.

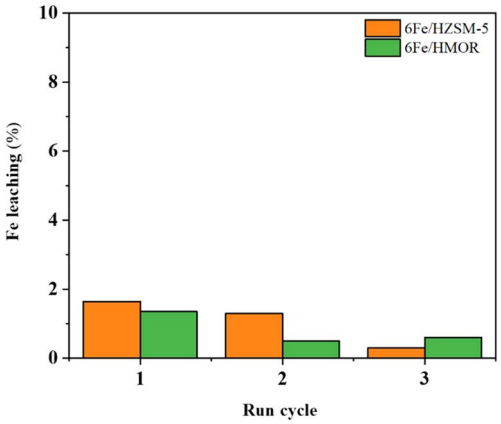

Fig. 17 Fe-leaching percent determined through three cycles of catalytic reaction.

cycles. Both catalysts exhibited a slight decrease in conversion over time, with 6Fe/HZSM-5 showing a slightly greater decline. However, the yields of 5-HMF produced by the 6Fe/HZSM-5 catalyst remained relatively constant and even increased somewhat during the second cycle. The repeated use of the catalyst may have resulted in slight surface roughening or pore opening, enhancing the contact between glucose and acid sites and thereby improving the efficiency of 5-HMF formation.

3.2.6 Characterization of the spent catalysts. The structures of the spent catalysts, 6Fe/HZSM-5 and 6Fe/HMOR, were characterized using XRD, as shown in Fig. 16(a and b). The intensity of the crystalline peaks corresponding to the HZSM-5 structure in the 6Fe/HZSM-5 catalyst was slightly reduced after repeated cycling. However, the intensity decreases from cycle 2 to cycle 3 was minimal. A similar trend was observed for the 6Fe/HMOR catalyst. Notably, mixed phases of HZSM-5 and HMOR were detected after the third cycle, indicating a phase transformation of the zeolite support in the 6Fe/HMOR catalyst over repeated use.

The changes in the zeolite structures were associated with a dramatic increase in coke formation on the catalyst during cycling, as determined by thermogravimetric analysis (TGA), as shown in Fig. 16(c and d). This result contrasted with that of the 6Fe/HZSM-5 catalyst, where coke formation was reduced over the course of the run. The FT-IR spectra of the spent catalysts show that the characteristic vibrations of the zeolite framework in the 6Fe/HZSM-5 and 6Fe/HMOR catalysts appear as bands at 1210 cm^{-1} and 1050 cm^{-1}. This observation confirms their

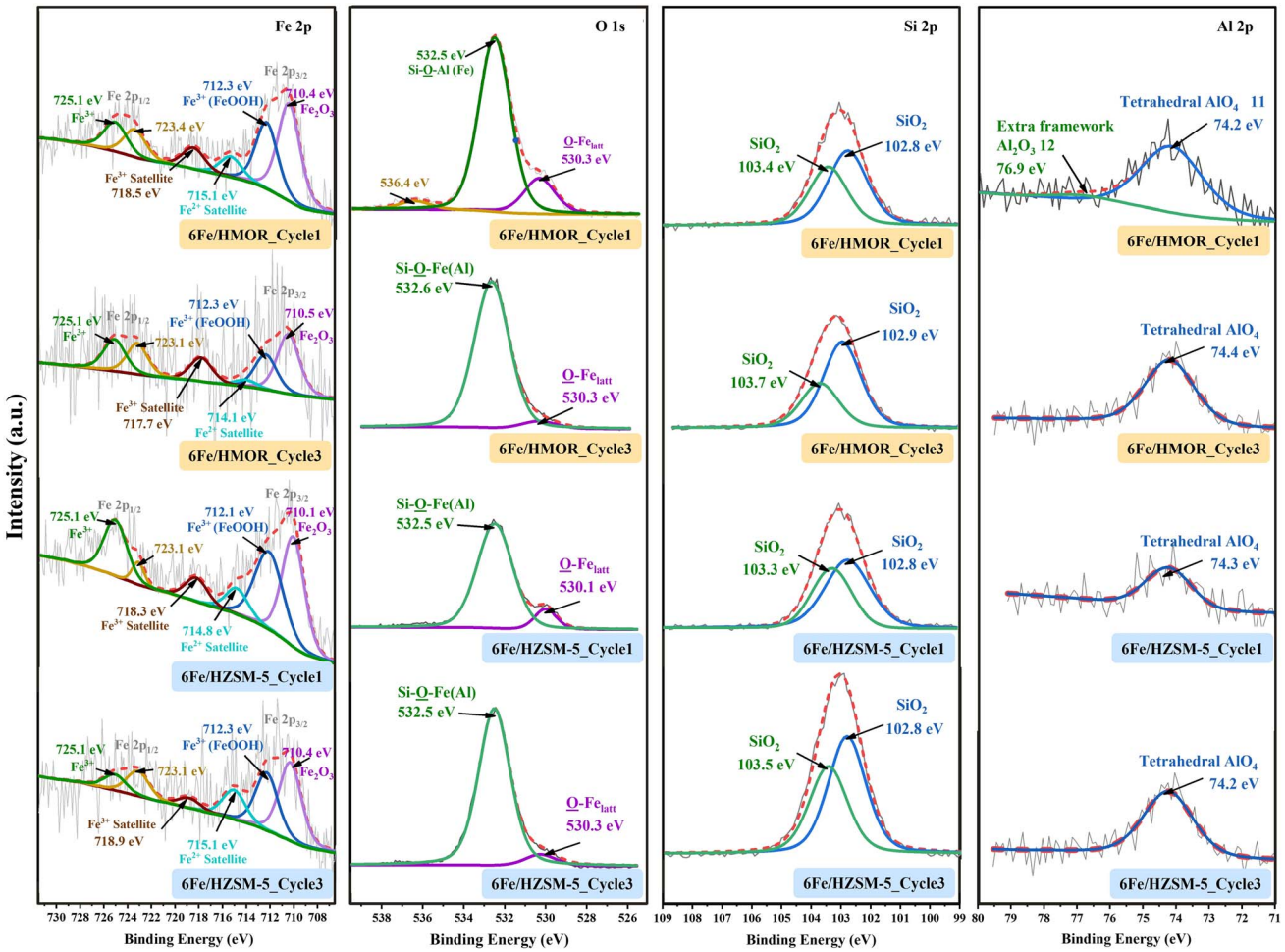

Fig. 18 XPS spectra of Fe 2p, O 1s, Si 2p, and Al 2p of Fe/HMOR and Fe/HZSM-5 spent catalyst.

structural stability, as illustrated in Fig. 16(e and f). However, there are slight changes in the intensity and position of the bands associated with surface hydroxyl groups and Brønsted acid sites, located at 3750 cm^{-1} and 3500 cm^{-1}, respectively. These changes indicate modifications or redistributions of the acid sites after the first reaction cycle for both catalysts.

Furthermore, the percentage of Fe leaching over the repeated use of the catalysts was below 2% (Fig. 17). The maximum leaching for both catalysts occurred during the first cycle and decreased over time.

XPS analysis of the spent 6Fe/HMOR and 6Fe/HZSM-5 catalysts after one and three reaction cycles confirms their excellent structural and chemical stability (Fig. 18). The Fe 2p spectra show no shift in binding energy or change in spectral features compared to the fresh catalysts, indicating that the iron oxidation state and coordination environment remain unchanged during reaction. In the O 1s region, a slight reduction of the Si–OH component was observed for 6Fe/HMOR after the first cycle, while the dominant Si–O–Si framework oxygen remained intact, suggesting only minor surface hydroxyl modification without framework degradation. The Si 2p spectra display exclusively the characteristic Si^{4+} signal of the SiO_2 framework, with no evidence of sub-oxide species (Si_2O_3), and no extra framework aluminum species were detected in Al 2p, indicating the absence of dealumination. Overall, these results demonstrate that the iron active sites and zeolite frameworks are well preserved after repeated catalytic cycles, confirming the durability and stability of the iron-supported zeolite catalysts.

4 Conclusions

This work demonstrates that glucose conversion to 5-HMF is controlled by the balance and nature of Brønsted and Lewis acid sites, which are strongly influenced by zeolite support and iron speciation. Characterization confirmed that Fe incorporation generates Fe-based Lewis acid sites (Fe_2O_3 and Fe_3O_4) together with Brønsted acid sites from framework Si–OH–Al, surface Fe–OH, and extra-framework Al–OH species, with Py-IR revealing a higher B/L ratio for Fe/HMOR than Fe/HZSM-5. Catalytic results in a biphasic *n*-BuOH/water system showed that moderate acidity and an optimized B/L ratio enhance 5-HMF selectivity while suppressing levulinic acid formation. XANES and UV-vis DRS established a strong correlation between Fe_3O_4-rich species and higher 5-HMF yields, as mixed-valence Fe^{2+}/Fe^{3+} provides moderate Lewis acidity that favors glucose isomerization, while excessive Fe_2O_3 leads to side reactions. The highest performance was achieved with 6Fe/HMOR at 190 °C, where synergistic Lewis–Brønsted acidity and controlled acid strength enabled efficient conversion of glucose to 5-HMF, providing clear guidance for rational catalyst design.

Author contributions

Tatchapol Nanmong led the conceptualization, catalyst synthesis, catalytic experiments, data analysis, and wrote the original draft. Waranya Obrom, Worapol Yingyuen, Tanawat Jaroenchur, and Phatteenan Thamthong contributed to catalyst preparation, catalytic testing, physicochemical and acid-site characterization, and data interpretation. Pimrapus Tawachkultanadilok, Yingyot Poo-arporn, Suttipong Wannapaiboon, and Narong Chanlek performed and supported advanced spectroscopic and synchrotron-based analyses. Jatuporn Wittayakun, Sanchai Prayoonpokarach, Bunyarat Rungtaweevoranit, Siriporn Kosawatthanakun, Pongtanawat Khemthong, and Jean-Paul Desaulniers contributed to methodology development, scientific discussion, and manuscript revision. Sirinuch Loiha supervised the project, acquired funding, and finalized the manuscript.

Conflicts of interest

There are no conflicts to declare.

Data availability

All data supporting the findings of this study are available within the article.

Acknowledgements

This work was supported by the Fundamental Fund of Khon Kaen University, the National Science Research and Innovation Fund (NSRF), the Center of Excellence for Innovation in Chemistry (PERCH-CIC), Southeast Asia-Europe Joint Funding Scheme (JFS) for Research and Innovation, Synchrotron Light Research Institute (SLRI), Nakhon Ratchasima, Thailand, NanoCatalysis and Molecular Simulation Research Group, National Nanotechnology Center (NANOTEC), Pratumthani, Thailand.

References

1 J. Fang, H. Dong and H. Xu, *Renewable Energy*, 2023, **218**, 119305.
2 C. Xu, Z. Miao, H. Zhao, J. Yang, J. Zhao, H. Song, N. Liang and L. Chou, *Fuel*, 2015, **145**, 234–242.
3 J. Li, S. Link and V. Hegelheimer, *J. Second Lang. Writ.*, 2015, **27**, 1–18.
4 S. Kang, J. Fu and G. Zhang, *Renewable Sustainable Energy Rev.*, 2018, **94**, 340–362.
5 I. K. M. Yu and D. C. W. Tsang, *Bioresour. Technol.*, 2017, **238**, 716–732.
6 A. Modak, A. R. Mankar, R. R. Sonde and K. K. Pant, *Renewable Energy*, 2023, **212**, 97–110.
7 M. Niakan, M. Masteri-Farahani, F. Seidi, S. Karimi and H. Shekaari, *React. Chem. Eng.*, 2023, **8**, 2473–2480.
8 M. Masteri-Farahani, M. Ghahremani and M. Niakan, *Energy Fuels*, 2025, **39**, 15225–15241.
9 M. Niakan, M. Masteri-Farahani and F. Seidi, *Renewable Energy*, 2023, **212**, 50–56.
10 M. Moreno-Recio, J. Santamaría-González and P. Maireles-Torres, *Chem. Eng. J.*, 2016, **303**, 22–30.

11 N. Senamart, S. Buttha, W. Pantupho, I. Koleva, S. Loiha, H. Aleksandrov, J. Wittayakun and G. Vayssilov, *J. Porous Mater.*, 2019, **26**, 1227–1240.
12 M. M. M. Kashbor, D. Sutarma, J. Railton, N. Sano, P. J. Cumpson, D. Gianolio, G. Cibin, L. Forster, C. D'Agostino, X. Liu, L. Chen, V. Degirmenci and M. Conte, *Appl. Catal., A*, 2022, **642**, 118689.
13 J. Bai, W. Ling, W. Chen, Y. Liu, P. Sun, H. Wang and C. Wang, *Mol. Catal.*, 2023, **541**, 113071.
14 G. Yang and L. Zhou, *Appl. Catal., A*, 2024, **677**, 119694.
15 B. R. Wood, J. A. Reimer and A. T. Bell, *J. Catal.*, 2002, **209**, 151–158.
16 R.-J. van Putten, J. C. van der Waal, E. de Jong, C. B. Rasrendra, H. J. Heeres and J. G. de Vries, *Chem. Rev.*, 2013, **113**, 1499–1597.
17 H. Xia, H. Hu, S. Xu, K. Xiao and S. Zuo, *Biomass Bioenergy*, 2018, **108**, 426–432.
18 S. Xu, L. Zhang, K. Xiao and H. Xia, *Carbohydr. Res.*, 2017, **446–447**, 48–51.
19 N. A. S. Ramli and N. A. S. Amin, *Appl. Catal., B*, 2015, **163**, 487–498.
20 Z. Wang, J. Zhang, W. Liu, Y. Wu and X. Liu, *ChemSusChem*, 2025, **18**, e202500344.
21 F. Xu, W. Chen, C. A. Walenta, C. R. O'Connor and C. M. Friend, *Chem. Sci.*, 2020, **11**, 2448–2454.
22 A. A. Marianou, C. M. Michailof, A. Pineda, E. F. Iliopoulou, K. S. Triantafyllidis and A. A. Lappas, *Appl. Catal., A*, 2018, **555**, 75–87.
23 L. Wang, J. Zhang, L. Zhu, X. Meng and F. S. Xiao, *J. Energy Chem.*, 2013, **22**, 241.
24 L. Fele Žilnik, M. Crnomarkovic, U. Novak, M. Grilc and B. Likozar, *Chem. Eng. Res. Des.*, 2023, **194**, 376–387.
25 J. Li, Y. Ma, L. Wang, Z. Song, H. Li, T. Wang, H. Li and W. Eli, *Catalysts*, 2016, **6**, 1.
26 Y. Su, G. Chang, Z. Zhang, H. Xing, B. Su, Q. Yang, Q. Ren, Y. Yang and Z. Bao, *AIChE J.*, 2016, **62**, 4403–4417.
27 C. Zhou, J. Zhao, A. E. A. Yagoub, H. Ma, X. Yu, J. Hu, X. Bao and S. Liu, *Egypt. J. Pet.*, 2017, **26**, 477.
28 J. Wang, J. Wang, H. Cui, Z. Li, M. Wang and W. Yi, *Fuel*, 2022, **321**, 124077.
29 P. Wrigstedt, J. Keskiväli and T. Repo, *RSC Adv.*, 2016, **6**, 18973–18980.
30 G. F. David, D. M. Delgadillo, G. A. Castro, D. C. Cubides-Roman, S. A. Fernandes and V. Lacerda Júnior, *Catalysts*, 2023, **13**, 574.
31 F. R. Tao, C. Zhuang, Y. Z. Cui and J. Xu, *Chin. Chem. Lett.*, 2014, **25**, 757.
32 Y. Xie, F. Yu, Y. Wang, X. He, S. Zhou and H. Cui, *Fluid Phase Equilib.*, 2019, **493**, 137–143.
33 B. Liu and Z. Zhang, *ACS Catal.*, 2016, **6**, 326–338.
34 C. Xu, E. Paone, D. Rodríguez-Padrón, R. Luque and F. Mauriello, *Chem. Soc. Rev.*, 2020, **49**, 4273–4306.
35 S. Singh, G. Hitkari and G. Pandey, *Nano-Met. Chem.*, 2019, **48**, 1–9.
36 A. W. Petrov, D. Ferri, M. Tarik, O. Kröcher and J. A. van Bokhoven, *Top. Catal.*, 2017, **60**, 123–130.
37 S.-H. Zhang, Y. H. Zhao, J.-K. Zhang, X.-Q. Feng, Q. J. Zhang and H. Wang, *Res. Chem. Intermed.*, 2024, **50**, 1–15.
38 A. Matloob, D. Radwan, L. Saad and S. Mikhail, *Inorg. Organomet. Polym.*, 2023, **33**, 254–265.
39 M. Thommes, K. Kaneko, A. V. Neimark, J. P. Olivier, F. Rodriguez-Reinoso, J. Rouquerol and K. S. W. Sing, *Pure Appl. Chem.*, 2015, **87**, 1051–1069.
40 Y. Murillo-Acevedo, L. Giraldo and J. C. Moreno-Piraján, *Microporous Mesoporous Mater.*, 2020, **304**, 109325.
41 H. D. Kim, H.-T. Song, A. Fazeli, A. Alizadeh Eslami, Y. S. Noh, N. Ghaffari Saeidabad, K.-Y. Lee and D. J. Moon, *Catal. Today*, 2022, **388–389**, 410–416.
42 Y. Li, L. Li and J. Yu, *Chem*, 2017, **3**, 928–949.
43 T. Ennaert, J. Van Aelst, J. Dijkmans, R. De Clercq, W. Schutyser, M. Dusselier, D. Verboekend and B. F. Sels, *Chem. Soc. Rev.*, 2016, **45**, 584–611.
44 G. G. Oseke, A. Y. Atta, B. Mukhtar, B. Y. Jibril and B. O. Aderemi, *Appl. Petrochem. Res.*, 2020, **10**, 55–65.
45 O. Travkina, M. Agliullin, R. Kuvatova, I. Pavlova, N. Narender and B. Kutepov, *Porous Mater.*, 2019, **26**, 995–1004.
46 T. Nawaz, S. Zulfiqar, M. Sarwar and M. Iqbal, *Sci. Rep.*, 2020, **10**, 10076.
47 N. Ben Younes, J. M. Ortigosa, O. Marie, T. Blasco and M. Mhamdi, *Res. Chem. Intermed.*, 2021, **47**, 2003–2028.
48 V. Harnchana, S. Chaiyachad, S. Pimanpang, C. Saiyasombat, P. Srepusharawoot and V. Amornkitbamrung, *Sci. Rep.*, 2019, **9**, 1494.
49 M. Khatamian, N. Afshar No, S. Hosseini Nami and S. Fazli-Shokouhi, *J. Iran. Chem. Soc.*, 2023, **20**, 1657–1670.
50 J. Domenzain-Gonzalez, J. J. Castro-Arellano, L. A. Galicia-Luna and L. Lartundo-Rojas, *Int. J. Photoenergy*, 2019, **2019**, 4981631.
51 H. Yang, B. Shi and S. Wang, *Catalysts*, 2018, **8**, 207.
52 J. Zhang, X. Tang, H. Yi, Q. Yu, Y. Zhang, J. Wei and Y. Yuan, *Appl. Catal., A*, 2021, **630**, 118467.
53 N. Chubar, V. Gerda, M. Micusik, M. Omastová, K. Heister, P. Man, G. Yablokova, D. Banerjee and J. Fraissard, *Acta Phys. Pol. A*, 2018, **133**, 1091–1096.
54 H. Tissot, L. Li, S. Shaikhutdinov and H.-J. Freund, *Phys. Chem. Chem. Phys.*, 2016, **18**, 25027–25035.
55 S. Senthilkumar, W. Zhong, M. Natarajan, C. Lu, B. Xu and X. Liu, *New J. Chem.*, 2021, **45**, 705–713.
56 F. S. Aguirre-Tostado, D. Layton, A. Herrera-Gomez, R. M. Wallace, J. Zhu, G. Larrieu, E. Maldonado, W. P. Kirk and M. Tao, *J. Appl. Phys.*, 2007, **102**, 084901–084907.
57 S. N. Moafor, P. K. Tsobnang, K. O. Oyedotun, R. Lontio Fomekong, G. L. Kabongo, M. Lebohang, J. N. Lambi and L. L. Jewell, *RSC Adv.*, 2023, **13**, 21393–21402.
58 R. Andreeva, E. Stoyanova, A. Tsanev and D. Stoychev, *Bulg. Chem. Commun.*, 2016, **48**, 96–102.
59 P. Tosuwan, S.-Y. Chen, H. Tateno, T. Mochizuki and A. Luengnaruemitchai, *Catal. Commun.*, 2022, **170**, 106488.
60 S. Xia, C. Wang, Y. Chen, S. Kang, K. Zhao, A. Zheng, Z. Zhao and H. Li, *Catalysts*, 2022, **12**, 1483.
61 Y. Xu, X. Yuan, M. Chen, A. Dong, B. Liu, F. Jiang, S. Yang and X. Liu, *J. Catal.*, 2021, **396**, 224–241.

62 F. Gao, Y. Zheng, R. Kukkadapu, Y. Wang, E. Walter, B. Schwenzer, J. Szanyi and C. Peden, *ACS Catal.*, 2016, **6**, 2939–2954.
63 M. Görgényi, J. Dewulf, H. Van Langenhove and K. Héberger, *Chemosphere*, 2006, **65**, 802–810.
64 H. Li, Q. Yi, Y. Shao, H. Xu, Z. Wang and Y. Liu, *Mater. Today Sustain.*, 2025, **31**, 101144.
65 L. F. L. Machado, L. S. Andrade, D. Mandelli and W. A. Carvalho, *ACS Omega*, 2024, **9**, 45328–45341.
66 J. A. Bennett, C. M. A. Parlett, M. A. Isaacs, L. J. Durndell, L. Olivi, A. F. Lee and K. Wilson, *ChemCatChem*, 2017, **9**, 1648–1654.